THE RELATIONSHIP OF MATERIAL PROPERTIES TO SEISMIC COUPLING
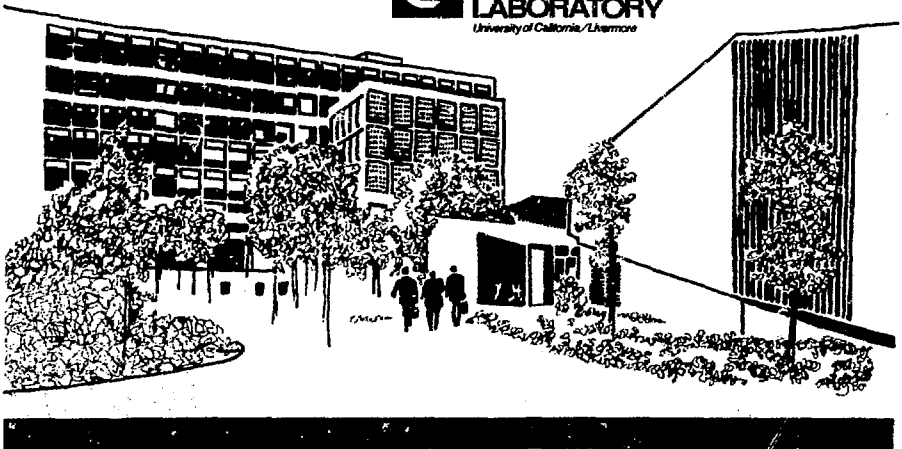
PART I: Shock Wave Studies of Rock and Rock-Like Materials

D. B. Larson

H. C. Rodean

March 5, 1975

LAWRENCE LIVERMORE LABORATORY
University of California/Livermore

LAWRENCE LIVERMORE LABORATORY
University of California/Livermore, California/94550

THE RELATIONSHIP OF MATERIAL PROPERTIES TO SEISMIC COUPLING

PART I: Shock Wave Studies of Rock and Rock-Like Materials

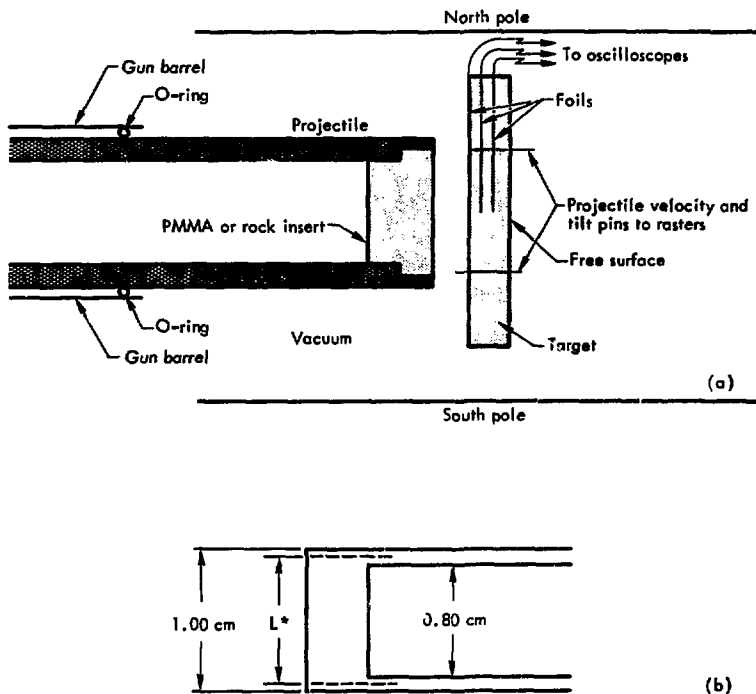D. B. Larson
H. C. Rodean

Contents

Fig. 1. (a) Schematic diagram of a gas gun experiment. The shock-wave due to impact travels through the target and is reflected at the free surface as an unloading wave. The lateral dimensions of the target are larger than the projectile and the target is thin compared to the projectile diameter to insure unperturbed recording until after the unloading has been completed at the gages. (b) Diagram illustrating the effective length L' of the brass foil used in the particle-velocity gage. The value as determined in four experiments is 0.899 cm ± 1%. The gage thickness is about 0.0025 cm.

interpretation. A second report (Part II) will cover the gas-gun data in detail, and will include a development of constitutive relationships.

In the gas-gun technique, flat-faced projectiles were accelerated with expanding helium gas and allowed to impact a target made up of plates of the test material (see Fig. 1). The shock wave produced by the impact loaded the target uniaxially while rarefaction from the free surface unloaded the material, also uniaxially. The gages sandwiched between the plates moved with the surrounding material.

The HE experiments employed a small (either 1.9×10^{-2} m or 9.5×10^{-3} m radius) sphere of LX04 HE as the energy

-3-

source. The charge was emplaced between plates of test material as indicated in Fig. 2. The diagnostic gages were placed between plates to give readings at various radial distances from the source.

The gages used were of two types: the first were thin (2.5 × 10^{-5} m) metal foils which moved perpendicular to the field produced by a large external electromagnet and provided particle velocity history; and the second were thin (1.8 × 10^{-4} m) piezoresistive ytterbium gages which provided stress history.

The particle velocity gage technique used in these experiments is ideal for studies in non-conductors. The gage element "rings" up to the material velocity in nanoseconds and follows the motion of the material as loading and unloading occur. In uniaxial flow, the gage element L does not change in length as motion occurs through the constant mag-

netic field B. Therefore, the particle velocity history $U_p(t)$ is proportional to the recorded emf, as described by the expression

$$U_p(t) = \frac{\epsilon(t)}{BL} \qquad (1)$$

where $\epsilon(t)$ is the time history of the emf. During the radial flow that occurs in the HE experiments, the gage element L is stretched. A correction for this effect is easily made, but in practice is small (the maximum value 0.5%) and was ignored.

Fig. 3. (a) Schematic of a ytterbium gage which is sandwiched in kapton or fiberglass. The total package thickness is about 0.018 cm. (b) Stress-time history recorded with a ytterbium stress gage.
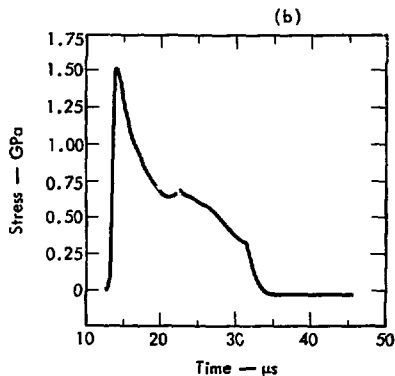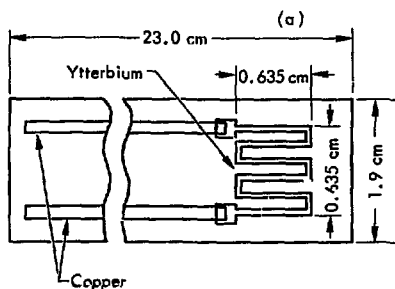

Fig. 2. Schematic of an HE experiment showing the gage elements emplaced radially from the HE source.

-4-

The piezoresistive ytterbium gage technique was developed at Stanford Research Institute,[7,8] and the piezoresistive response has been related to stress by Ginsberg[8] and Spataro.[9] Unfortunately ytterbium follows different paths during loading and unloading for stress levels above approximately 0.15 GPa. This leads to an offset in the recorded signal and requires a separate set of calibrations for unloading. Because of the inherently larger scatter in stress gage data and additional uncertainties in defining the unloading path, these gages were not used in the uniaxial experiments. However, in radial flow valuable additional data describing the stress deviator and the material moduli are available if both stress and particle-velocity histories are measured simultaneously. Consequently, both gage types were used on most HE experiments. Figure 3 shows the stress gage design along with a record from an HE experiment.

IV. Experimental Results

GAS-GUN EXPERIMENTS

The gas-gun technique was used to obtain uniaxial flow-data on all thirteen materials listed in Section II. The acquired data were in the form of particle velocity histories. To convert these records (for example see those shown in Fig. 4) to equation-of-state data requires expressions relating particle velocity history to the material properties of interest. The desired relationships can be obtained from expressions for the conservation of mass and linear momentum. For uniaxial flow, the conservation equations are

$$\left(\frac{\partial \rho}{\partial t}\right)_h + \rho\left(\frac{\partial U_p}{\partial x}\right)_t = 0 \tag{2}$$

$$\rho\left(\frac{\partial U_p}{\partial t}\right)_h + \left(\frac{\partial \sigma}{\partial x}\right)_t = 0 \tag{3}$$

where ρ is the density, σ the stress in the direction of compression, U_p the particle velocity, x the Eulerian coordinate, h the Lagrangian coordinate and t the time. Since the particle velocity is

measured at a constant Lagrangian coordinate, the Eulerian coordinate is eliminated from these expressions by using the identity for uniaxial flow,

$$\left(\frac{\partial h}{\partial x}\right)_t = \rho / \rho_0$$

where ρ_0 is the initial or reference density. Using this substitution and the identities

$$C_{U_p}\left(\frac{\partial t}{\partial U_p}\right)_h \left(\frac{\partial U_p}{\partial h}\right)_t - C_\sigma\left(\frac{\partial t}{\partial \sigma}\right)_h \left(\frac{\partial \sigma}{\partial h}\right)_t = -1$$

where

$$C_{U_p} = \left(\frac{\partial h}{\partial t}\right)_{U_p} \text{ and } C_\sigma = \left(\frac{\partial h}{\partial t}\right)_\sigma ,$$

we obtain

$$\left(\frac{\partial V}{\partial U_p}\right)_h = \frac{V_0}{C_{U_p}} \tag{4}$$

$$\left(\frac{\partial \sigma}{\partial U_p}\right)_h = \rho_0 C_\sigma \tag{5}$$

where $V = 1/\rho$ is the specific volume. For steady loading waves (i.e., a shock

front), $C_\sigma = C_{U_p} = U_s$ (a constant) and Eqs. (4) and (5) can be integrated across the steady wave to give the so called "jump conditions"

$$\frac{V - V_0}{V_0} = \frac{U_p}{U_s} \qquad (6)$$

$$\sigma - \sigma_0 = \rho_0 U_p U_s . \qquad (7)$$

In these equations, U_s is the steady wave velocity or shock velocity. For general non-steady flow, C_σ and C_{U_p} are functions

of U_p; thus Eqs. (4) and (5) must be integrated numerically using recorded data (both stress and particle velocity) at two or more Lagrangian points. For simple waves,[*] C_σ and C_{U_p} are equal and Eqs. (4) and (5) can be integrated numerically using only particle velocity histories. Furthermore, the initial value of C_{U_p} on

_____
[*] A simple wave is a flow pattern in which the characteristics are straight lines in the x, t plane and the thermodynamic variables are a function of particle velocity alone.
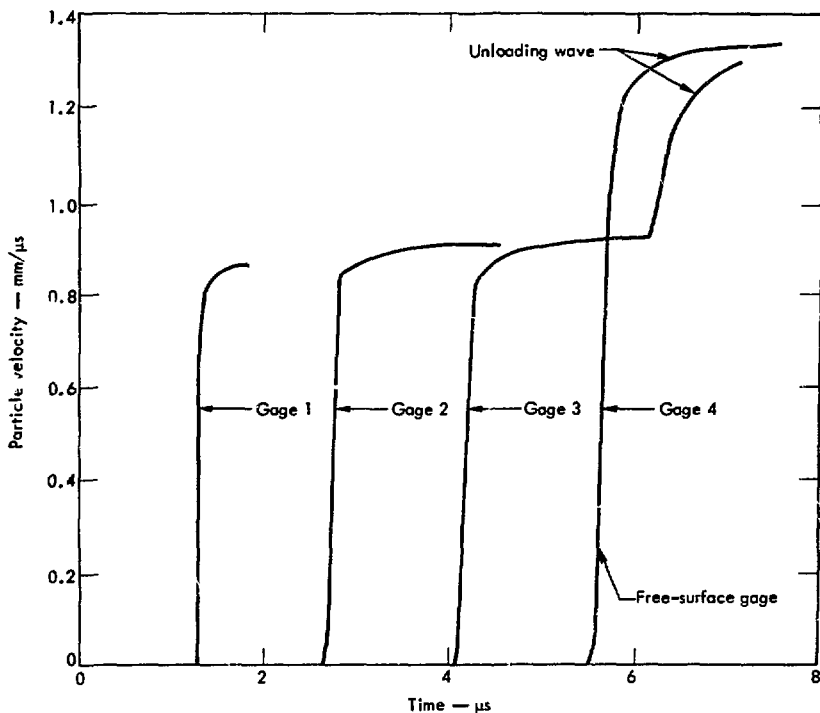

Fig. 4. Particle-velocity time profiles observed in dry Mt. ⌐len tuff. The gages were approximately 3 mm apart, with Gage 1 at the .)act surface and Gage 4 at the free surface.

the unloading cycle is related to the longitudinal sound speed C at that compression by the following equation:

$$C(U_p) = C_{U_p}(U_p)\rho_0 V. \qquad (8)$$

For a detailed discussion of this gage analysis, see Refs. 10 and 11.

Data based upon this analysis and assuming simple waves are presented in the following paragraphs.

PMMA

PMMA, polymethylmethacrylate, although not an earth material, was selected for study because it is well characterized,[12,13] is readily available, and is transparent. These properties have allowed a calibration of the gage techniques and the use of optics to establish the sphericity of the high-explosive source. The PMMA chosen was manufactured by
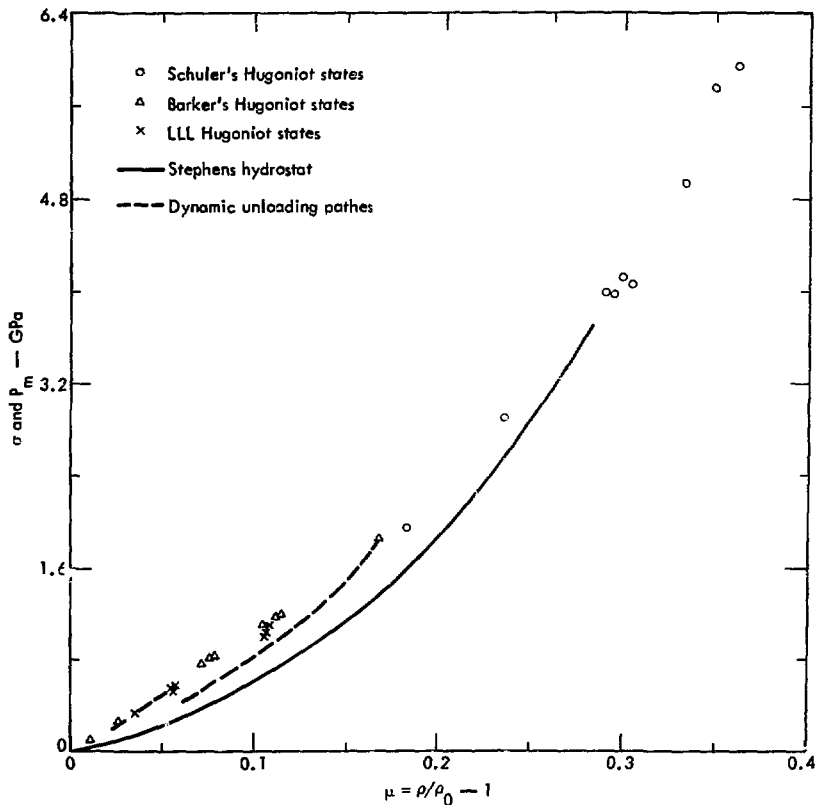

Fig. 5. A comparison of shock-wave and quasihydrostatic compression data for PMMA.

Rohm and Haas,[*] and has an initial density of 1.18 Mg/m³.

Figure 5 shows available Hugoniot states, several loading-unloading paths and a curve derived from hydrostatic and

quasihydrostatic loading.[14] The behavior is characteristic of a strain-rate-sensitive elastic-plastic material which yields at stress levels above approximately 7 GPa.[12,13] Figure 6 compares longitudinal sound speed derived using Eq. (8) with those determined acoustically. Good agreement in speeds, indicated by the dotted line, results from adjusting the specific volumes of the acoustic data to

[*]Reference to a compnay or product name does not imply approval or recommendation of the product by the University of California or the U. S. Energy Research and Development Administration to the exclusion of others that may be suitable.
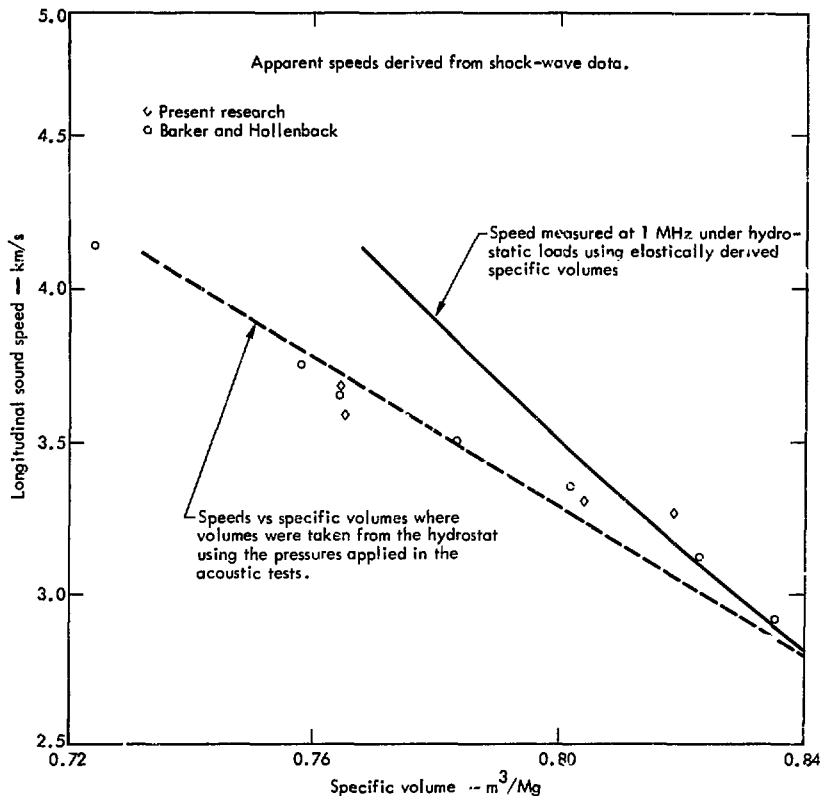

Fig. 6. Comparison of longitudinal sound speed derived using Eq. (8) with those determined acoustically.
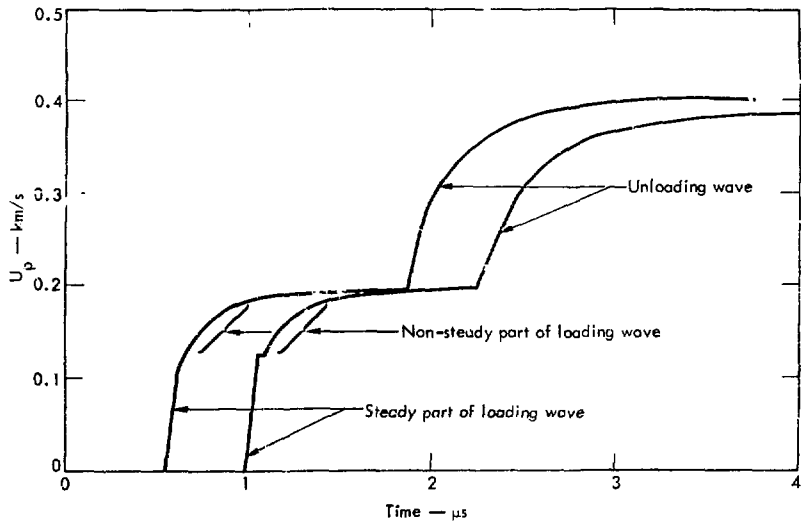
Fig. 7. Particle-velocity time profiles for Blair dolomite. Both the loading and un-
loading waves spread out as they propagate.

agree with hyarostatic tests rather than
using elastically derived values.

Figure 5 shows a separation of about
0.3 GPa between the hydrostat and the
Hugoniot up to stress of approximately
3 GPa. Beyond 3 GPa, the two sets of
data seem to merge. If this separation
is interpreted as a measure of shear
strength, the data suggests a loss of
strength at shock states above approxi-
mately 4 GPa.

Blair Dolomite

Blair dolomite is a fine-grained (70-
80% <10 μ and 20-30% averaging ~0.5 mm)[15]
dolomite [Ca Mg $(CO_3)_2$] from Berkeley
Co., West Virginia. The measured bulk
density is 2.84 Mg/m^3 and the porosity
is less than 1% based on the x-ray density
of dolomite.

Uniaxial gas-gun experiments were
conducted using the design shown in
Fig. 1 with PMMA projectile inserts for
the lower four stress levels and dolomite
inserts for the higher two stress levels.
Each target assembly consisted of three
dolomite plates with a particle velocity
gage at each interface. A typical set of
records is shown in Fig. 7. Both loading
and unloading waves are unsteady (i. e.,
they spread as they propogate). The
wave shapes are similar to PMMA, and
indicate that dolomite is strain-rate sen-
sitive. Figure 8 shows a typical loading-
unloading cycle and the various experi-
mental Hugoniot states. The measured
hydrostat for Blair dolomite is included
for comparison.[16] Figure 8 also shows
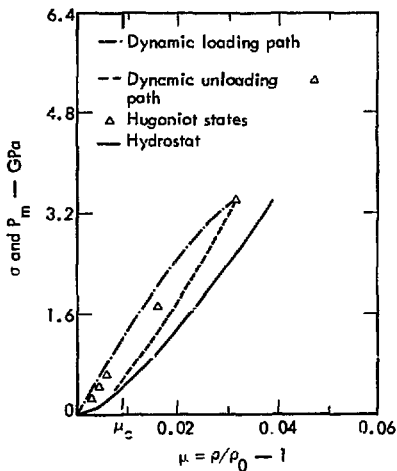the μ corresponding to crystal density μ_c.
It appears that the dynamic unloading

Fig. 8. A comparison of shock-wave and quasihydrostatic compression data for Blair dolomite.

Fig. 9. Comparison of shock-wave-derived sound speeds with the longitudinal sound speeds measured ultrasonically in Blair dolomite.

states are approaching crystal density as the loading stress is increased. This suggests that the hysteresis might be associated with pore collapse.

The separation between the hydrostat and the Hugoniot states give shear strengths that agree with quasi-static triaxial data. In Fig. 9 sound speeds derived from the shock data are compared with ultrasonic measurements. These data are also in good agreement.

Westerly Granite

The Westerly granite used was of the blue variety from the Bonner Monument Co., Westerly, Rhode Island. The bulk density is 2.65 Mg/m^3 with a porosity of <1%.

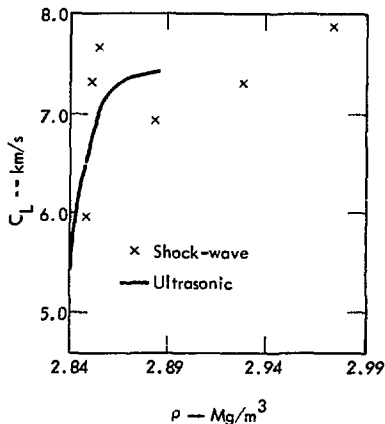The experiments were designed in a manner similar to the dolomite experi-

ments. As Fig. 10 shows, the loading wave profile is steady. This leads to a straight line loading in the σ-μ plane and as Fig. 11 shows, the unloading is essentially along this same line. Thus granite is, to a first approximation, elastic over the stress interval of these uniaxial compression experiments (i.e. to at least 4.2 GPa). The variation in loading wave shock velocity as a function of stress implies some deviation from elastic behavior. This is probably associated with closing of microcracks and grain boundary effects. The hydrostat for Westerly granite is plotted in Fig. 11 for comparison.[17]

Figure 12 gives a comparison of longitudinal sound speed determined from ultrasonic measurements[17] and those determined from the shock-wave data using Eq. (8).
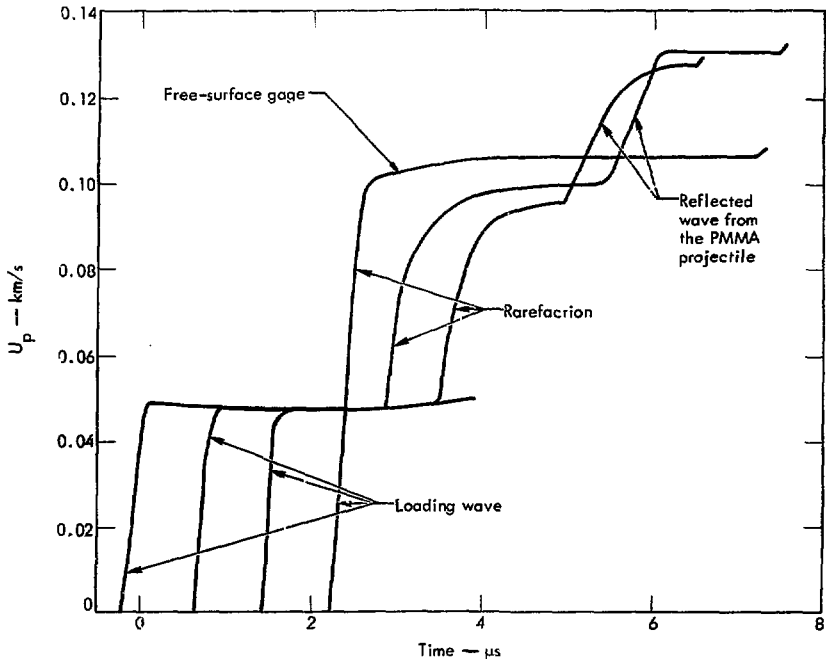
-10-

Fig. 10. Particle-velocity time profiles in Westerly granite.

Nugget and Wagon Wheel Sandstone

Two sandstones were studied under uniaxial flow: Nugget sandstone from Utah and Wagon Wheel sandstone from Sublette Co., Wyoming. Only one, Nugget, was used in the HE experiments. The Nugget is nominally 90% quartz with an average bulk density of 2.55 Mg/m^3 and porosity of approximately 3%. The Wagon Wheel is a graywacke with an average density of 2.38 Mg/m^3 and approximately 10% porosity.
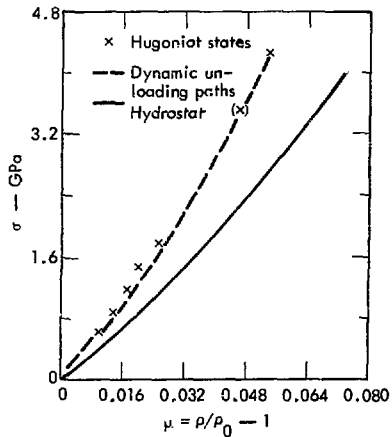
Fig. 11. A comparison of shock-wave and quasihydrostatic compression data for Westerly granite.

× Hugoniot states
--- Dynamic un-
loading paths
— Hydrostat (×)

$\mu = \rho/\rho_0 - 1$

-11-

Several gas-gun experiments were carried out on each sandstone. For the Nugget, the loading wave profiles were essentially steady for all stress levels. However, the Wagon Wheel profiles were non-steady once the 0.6-0.8 GPa stress level was reached. Since the Wagon Wheel has 10% porosity, the non-steady
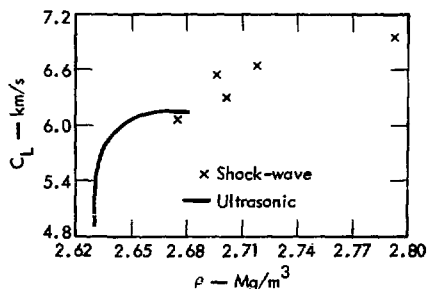

Fig. 12. A comparison of shock-wave-derived sound speeds with acoustic values in Westerly granite.

flow is associated with collapse of pores and the 0.6-0.8 GPa stress level is associated with the threshold for matrix failure. Figure 13 shows the wave profiles for one experiment in Nugget sandstone. Figure 14 gives a comparison of shock states for both materials while Figure 15 gives the shock wave data on Nugget sandstone compared with the hydrostat.[18] Figure 16 compares longitudinal sound speeds determined from Eq. (8) to those measured acoustically.[18]

From Fig. 13, it appears that the Nugget sandstone loses very little of its porosity upon compression to 1.6 GPa, although the data suggests that some micro-cracks are closed at low stress. However, the unloading data show that the Wagon Wheel sandstone has a definite loss of porosity once the 0.6-0.8 GPa level is exceeded.

The disagreement between sound speed at higher compressions shown in Fig. 16 is surprising.
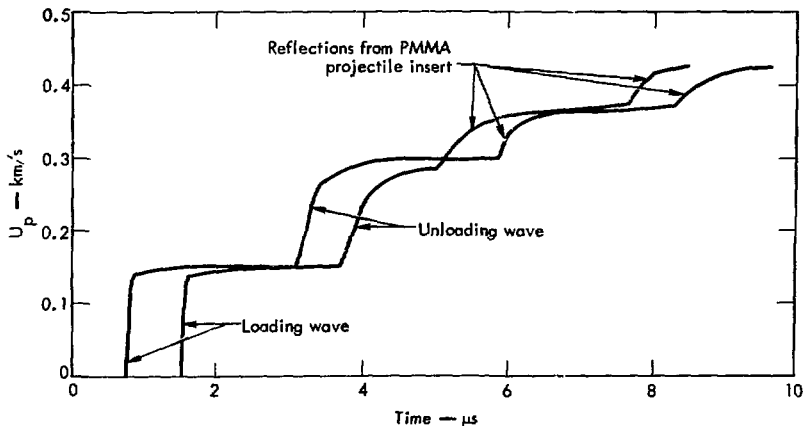

Fig. 13. Particle-velocity time histories in Nugget sandstone under uniaxial strain conditions.
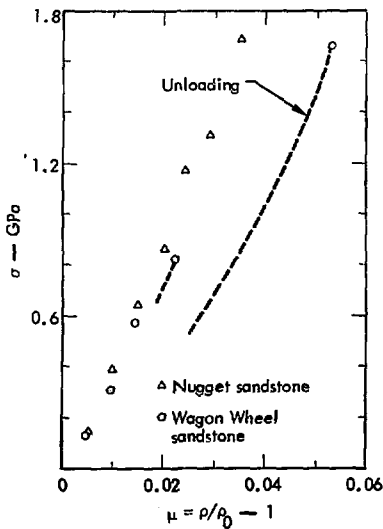
Fig. 14. A comparison of shock-wave Hugoniot data for Wagon Wheel and Nugget sandstones.
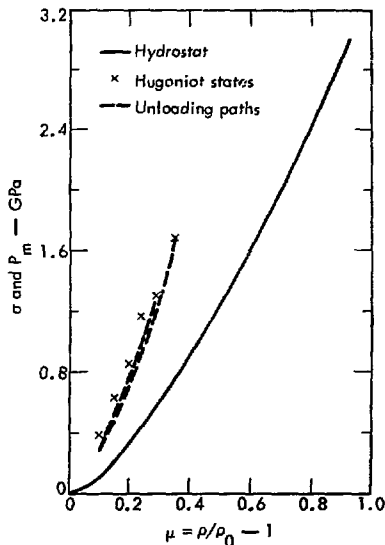

Fig. 15. A comparison of shock-wave and quasihydrostatic compression data for Nugget sandstone.

Salt

Fine-grained Leslie salt was pressed isostatically for 1 hr at 120°C using 0.14 GPa of pressure. This procedure produced large cylindrical samples (0.4 m diameter by 0.6 m high) of density 2.13 Mg/m^3. Since crystal density for sodium chloride is 2.165 Mg/m^3, this indicates a porosity of 1.6%.

Three gas-gun experiments were conducted using samples machined from the large cylinders. The particle velocity records show two loading waves. The first wave is probably associated with mechanical yielding. The following wave shows a slight non-steady behavior, indicating some strain-rate dependence. Figure 17 gives the complete loading-

unloading cycle determined from analysis of the data. Figure 17 also shows the μ corresponding to crystal density, μ_c. From the path of the unloading it appears that all of the porosity was eliminated in the loading process to 1.0 GPa. Subsequent tests to lower final loading states will be used to establish a relationship between pore elimination and stress.

Dry and Water-Saturated Mt. Helen Tuff

Mt. Helen tuff is a fine-grained, highly porous rock found near Mt. Helen in southern Nevada. The dry rock has erage measured density of 1.46 Mg/m^3 and a porosity of 38%. The grain density is 2.32 Mg/m^3 and the average measured saturated density is 1.84 Mg/m^3.

-13-
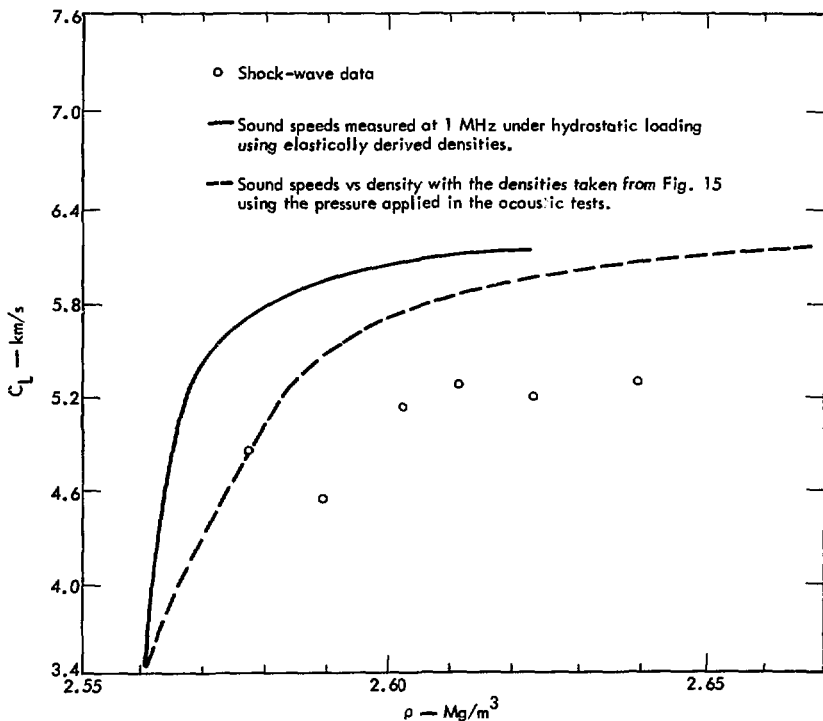
Fig. 16. A comparison of shock-wave and acoustically-derived sound speeds for Nugget sandstone.

These data imply that all pores are open and accessible to water saturation.

Uniaxial shock-wave loading experiments were conducted using both materials. The saturated samples were contained in a special vacuum-sealed target holder shown in Fig. 18. Figures 19 and 20 show the resulting compression data, the hydrostat,[19] and some ultra-high stress states obtained by SRI.[20]

Fig. 17. Shock-wave data for polycrystalline salt.

-14-
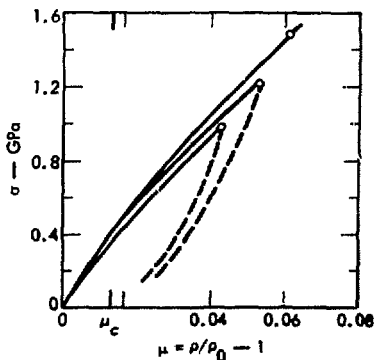
Fig. 18. Schematic of the setup for the dynamic equation-of-state experiments with water-saturated samples. The PMMA buffer plate and vacuum plate are used to isolate the sample from the gas-gun vacuum. The foil at the PMMA-sample interface records the input particle velocity. The other gages record the particle-velocity history when the sample is first loaded and then unloaded as the shock waves rarefy at the free surface.

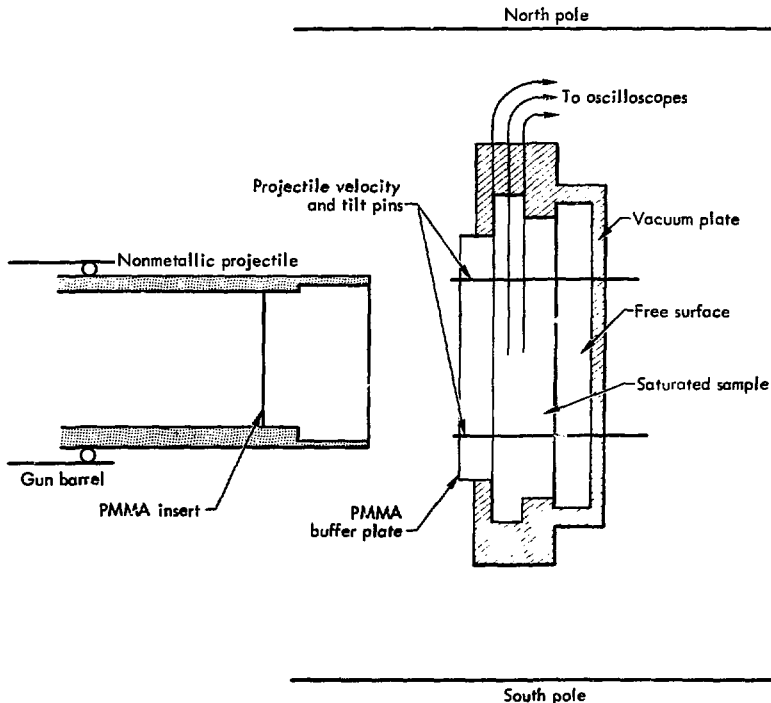The saturated data are consistent with a material that is both insensitive to strain rate and has very little shear strength. The absence of strain-rate effects is suggested by the steady-wave loading profiles that propagate through the samples. The small shear strength is suggested by the close proximity of the uniaxial loading data and the hydrostat, since the separation of these curves beyond the elastic limit, assuming an isotropic solid, is given by

$$\sigma - P_m = \frac{4}{3}\tau \qquad (9)$$

where τ is the resolved shear stress and P_m is the mean pressure.

The behavior of dry porous tuff is very different from saturated tuff in that there appears to be little correlation between dynamic and hydrostatic data. The high strain-rate uniaxial loading is non-steady as Fig. 4 shows, and the crossing of the

-15-

two loading curves in Figs. 19 and 20 near 1.3 GPa suggests extensive shear-induced compaction with uniaxial loading.

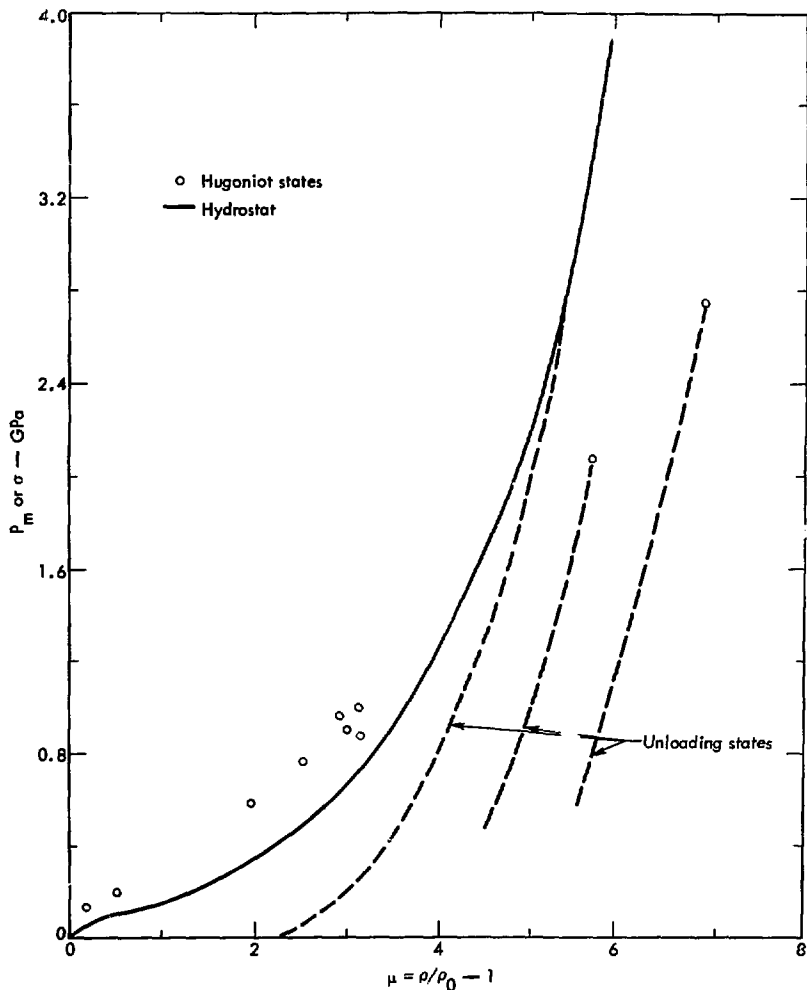Indiana limestone was obtained from the Indiana Limestone Co. of Bedford,

Fig. 19. A comparison of shock-wave and quasihydrostatic data for dry Mt. Helen tuff.

Indiana. It is a calcite cemented stone formed of shells and shell fragments. The rock is >90% $CaCO_3$ having an average dry bulk density of 2.28 Mg/m^3 and an average saturated density of 2.46 Mg/m^3. The measured porosity is 18% which implies that within measurement errors all pores are connected.

The gas-gun experiments on saturated samples were carried out using the scheme shown in Fig. 18. However, the relative velocities of the two waves propagating in the dry limestone samples required the use of a thin projectile insert of PMMA backed by low-density foam as the source of unloading in order to complete the loading before unloading reached the downstream gage. Figure 21 gives some typical wave profiles for dry samples. The precursor wave is believed to be associated with failure while the relatively slow buildup to the Hugoniot state is thought to be due to rate-dependent pore collapse. The subsequent drop in particle velocity is due to rarefaction from the projectile side. Figure 22 gives comparisons of Hugoniot states and the hydrostat.[21] Some unloading paths are also included. Figure 23 gives this same comparison for saturated limestone and Fig. 24 includes the Hugoniot states measured by SRI.

The results for both dry and saturated Indiana limestone are quite different from those for dry and saturated Mt. Helen tuff. The dry limestone shock-loading paths remain above the hydrostat for all stress levels (see Fig. 24). This suggests the absence of shear-enhanced compaction or the presence of some competing effect. The two saturated materials are also somewhat different

in behavior. The saturated limestone produces non-steady wave profiles which, as Fig. 23 shows, give rise to loading paths that lie above the hydrostat at low stresses. However, the higher stress data seem to lie along the hydrostat.

Frozen Materials

The frozen materials studied, except for polycrystalline ice, were obtained from the U. S. Army Cold Regions Research and Engineering Laboratory (CRREL), Hanover, New Hampshire.
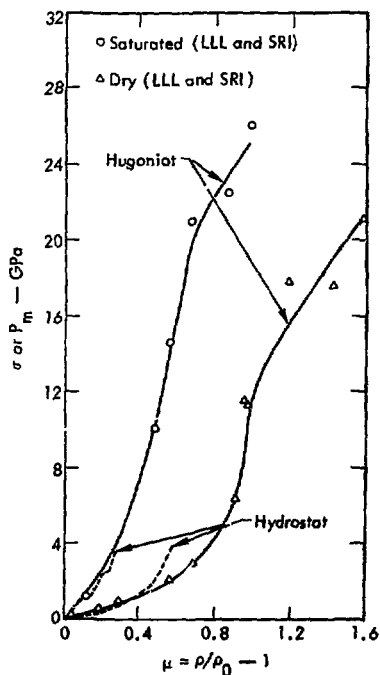

Fig. 20. A comparison of shock-wave and quasihydrostatic data for both dry and saturated Mt. Helen tuff.
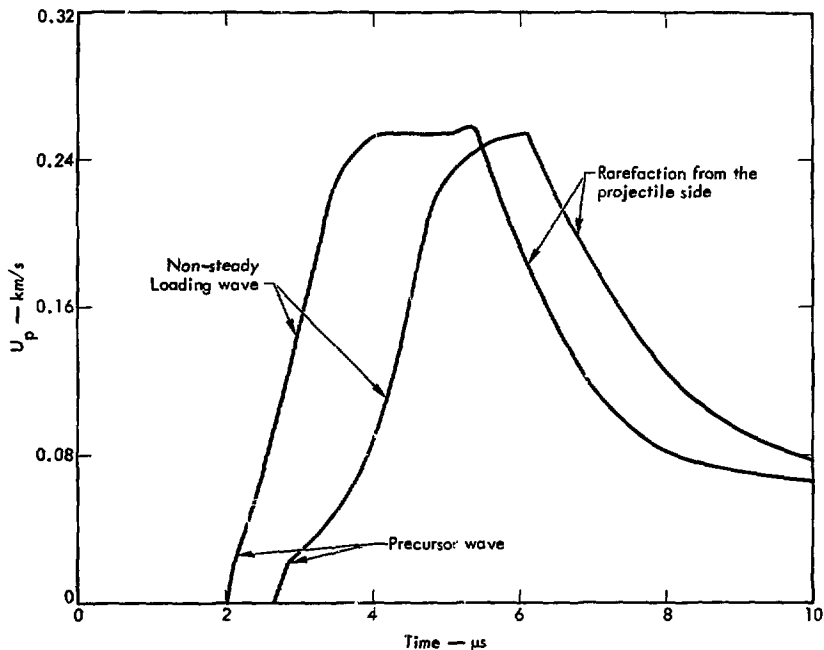
-17-

Fig. 21. Particle-velocity time histories in dry Indiana limestone.

The polycrystalline samples were made from large blocks of commercial ice. The single-crystal samples, both a- and c-axis oriented, were obtained from Dr. Itagaki of CRREL. The frozen soils were frozen directionally to maintain soil-grain contact. One, West Lebanon glacial till, had a dry density of 1.86 Mg/m^3 and an expected saturation density of 2.21 Mg/m^3. The average sample density was 2.08 Mg/m^3. The second, Ottawa banding sand, had a dry density of 1.65 Mg/m^3, a saturated density of 2.03 Mg/m^3, and an average sample density of 2.03 Mg/m^3. Porosity in both materials was about 35%.

Experiments on single-crystal samples were conducted to measure the effect of orientation (i. e., shear strength) on the behavior. Figure 25 shows the experimental configuration and Fig. 26 gives wave profiles measured in one such experiment. The first wave is interpreted as due to the onset of melting, and the non-steady flow that follows is attributed to strain-rate effects associated with transformation kinetics. Figure 27 shows results from analysis of single-crystal data along with a quasi-static -10°C isotherm.[22] No orientation effects consistent with experimental uncertainty were detected. For more detail, see Ref. 23.

Figure 28 gives typical wave profiles observed in samples of frozen soil. The precursor wave is associated with the onset of melting of the interstitial ice. The non-steady behavior of the second wave is associated with transformation kinetics. The separation between the hydrostat and the Hugoniot states is
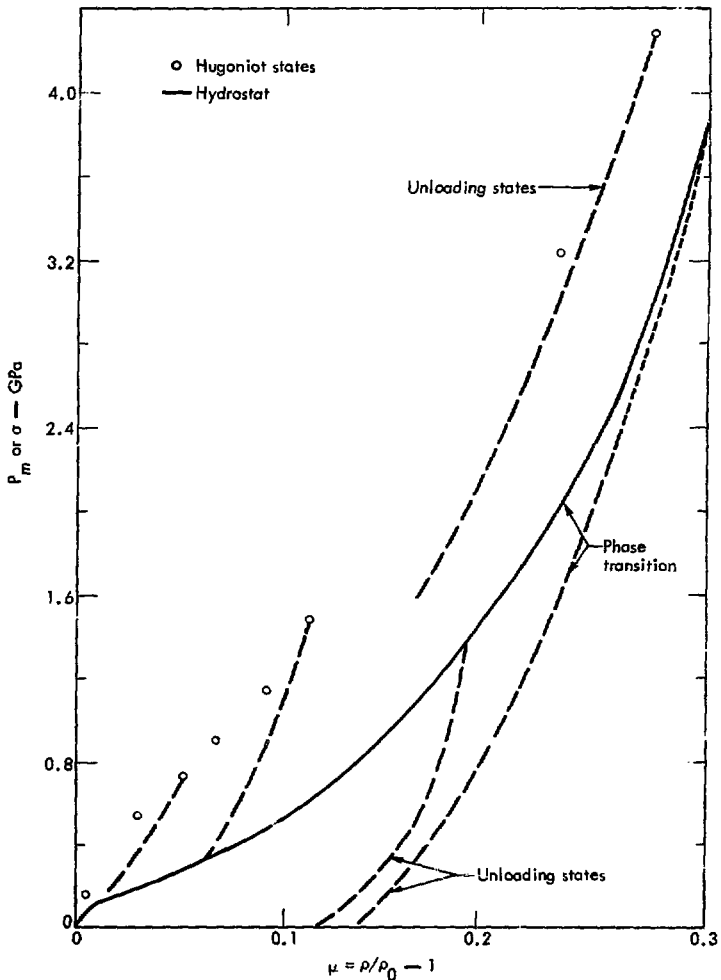

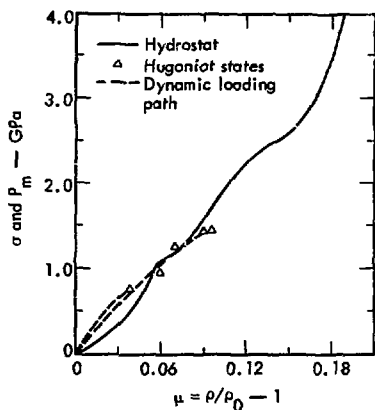Fig. 22. Comparison of dynamic and quasihydrostatic data for dry Indiana limestone.

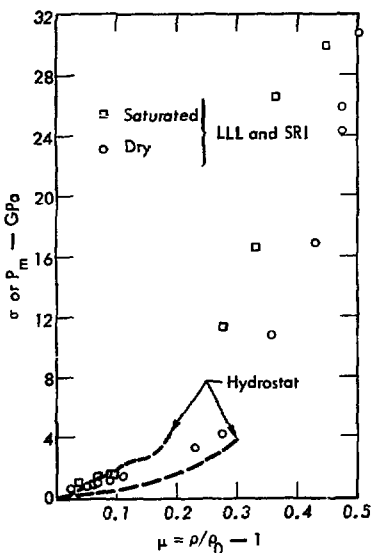Fig. 23. Comparison of dynamic and quasihydrostatic data for saturated Indiana limestone.

Fig. 24. Comparison of shock-wave and quasihydrostatic data for dry and saturated Indiana limestone.

probably due to strain-rate effects associated with the transformation rather than to shear stress. Figures 29-33 give the stress-volume data for polycrystalline ice, and for the frozen soils.

Comparison of Figs. 26 and 28 show the major difference between the frozen soil and ice profiles to be the dispersion in the precursor wave. This difference is probably associated with different transformation kinetics which result from complex thermodynamics caused by two-component interactions in the frozen soils.

SMALL-SCALE HE EXPERIMENTS

Data from the various HE experiments and the gas-gun experiments described earlier were converted to particle-velocity and stress-time histories using GANDALF, our interactive version of the SRI Lagrange-Gage Code.[24] The stress-time histories were corrected for hysteresis in unloading using the experimental results of Ginsberg[8] and algorithms developed by Hearst.[25]

PMMA

The experimental results for PMMA are given in Table 1 and in Figs. 34-36. No stress-time histories were measured in PMMA, but Fig. 34 gives representative particle-velocity-time histories at various distances from the source. The flattening of these particle-velocity records at late times for $R/R_0 > 10$ (R_0 is the radius of the HE source and R is the distance from the center of the HE to the gage prior to detonation) indicates that the gages were in free-flight. At post-shot time, the plate these gages were attached to was recovered undamaged
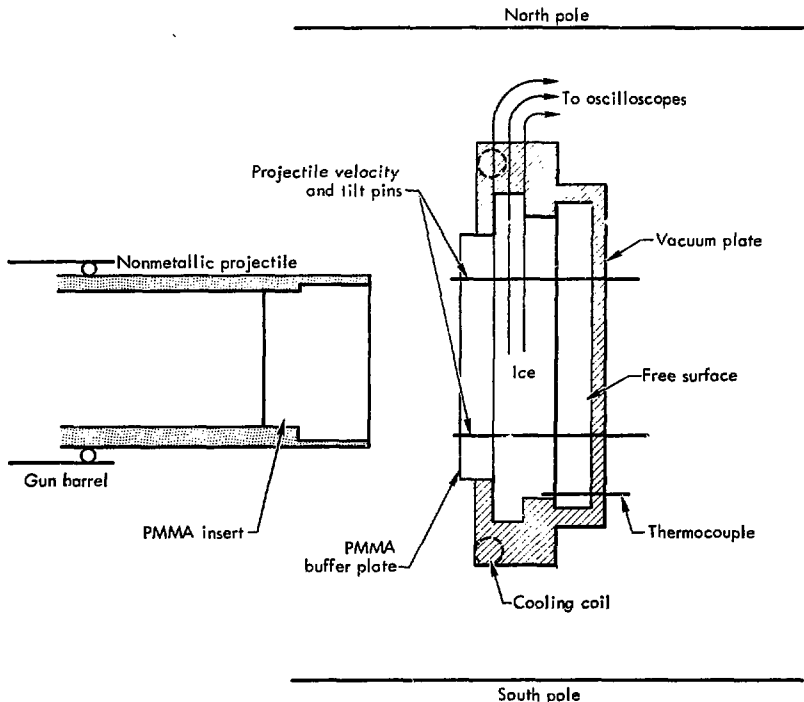
-20-

Fig. 25. Schematic of the setup for the dynamic equation-of-state experiments with ice samples. The temperature is maintained at -10 ± 1°C by the controlled circulation of cold N_2 vapors through the cooling coil. The Plexiglas buffer plate and vacuum plate are used to insulate the ice surfaces. The foil at the PMMA ice interface records the input particle velocity. The other two gages record the particle-velocity history when the ice is first loaded and then unloaded as the shock waves rarefy at the free surface.

while plates on either side were broken. This suggests spalling of the plate at the interface due to tensile failure of the epoxy bonds holding the plates together. Figure 34 gives the decay of peak particle-velocity as a function of scaled distance. These data indicate a decay proportional to $R^{-1.6}$ for stresses above approximately 0.7 GPa and $R^{-1.25}$ below. In Fig. 36, time-of-arrival measurements

are used to calculate average shock velocities between gages. These are correlated with expected shock velocities based on Barker's[13] measured shock-velocity — particle velocity results.

Blair Dolomite

The high-explosive data for Blair dolomite is shown in Table 2 and Figs. 37 and 38. Figure 37 shows the particle-velocity-time
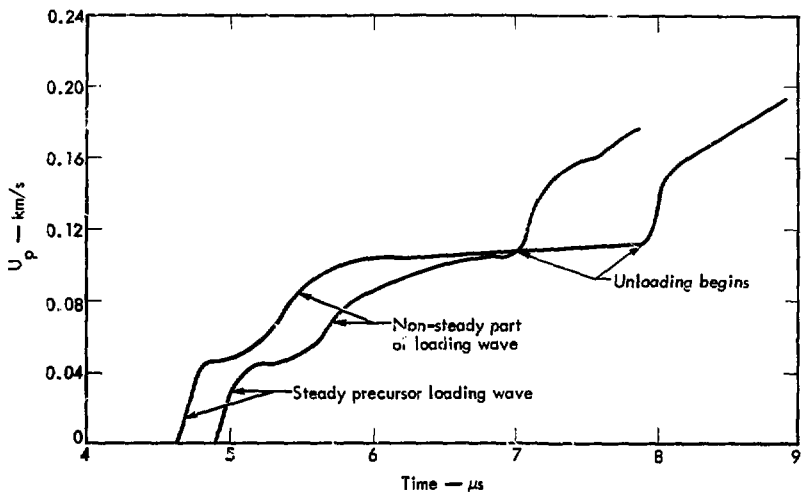
-21-

Fig. 26. Particle-velocity time histories in single-crystal ice. The loading was along the B-axis.
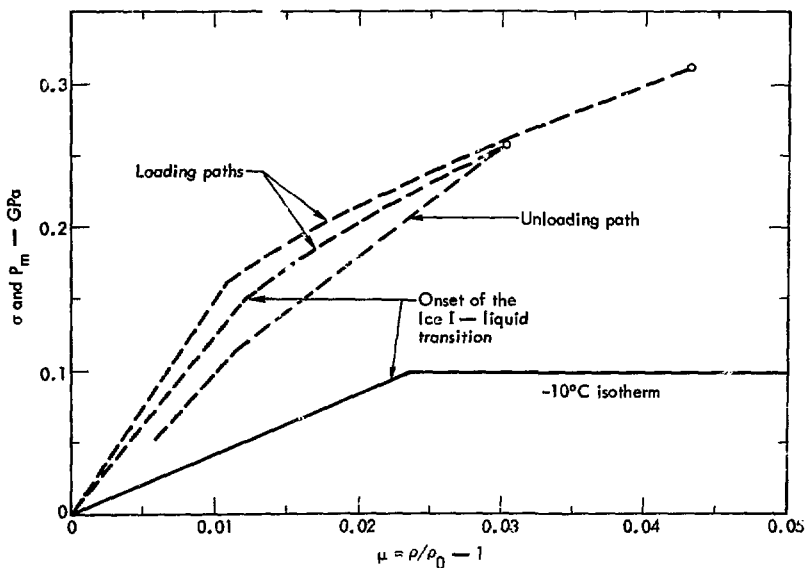

Fig. 27. A comparison of typical shock-wave data in single-crystal ice with the -10° isotherm.
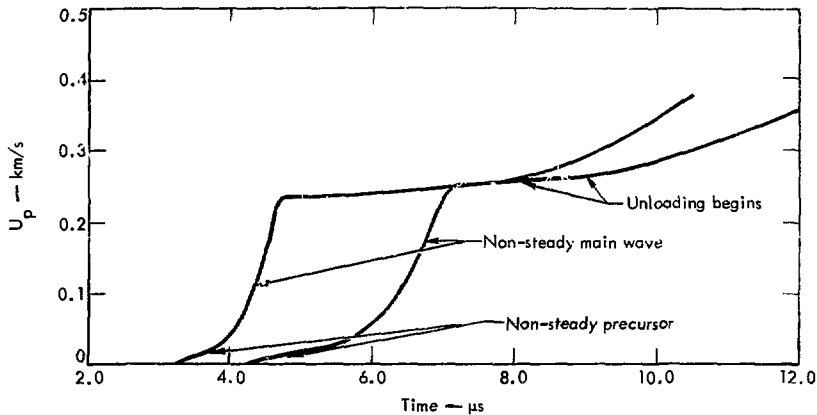
Fig. 28. Particle-velocity time histories in frozen West Lebanon glacial till.
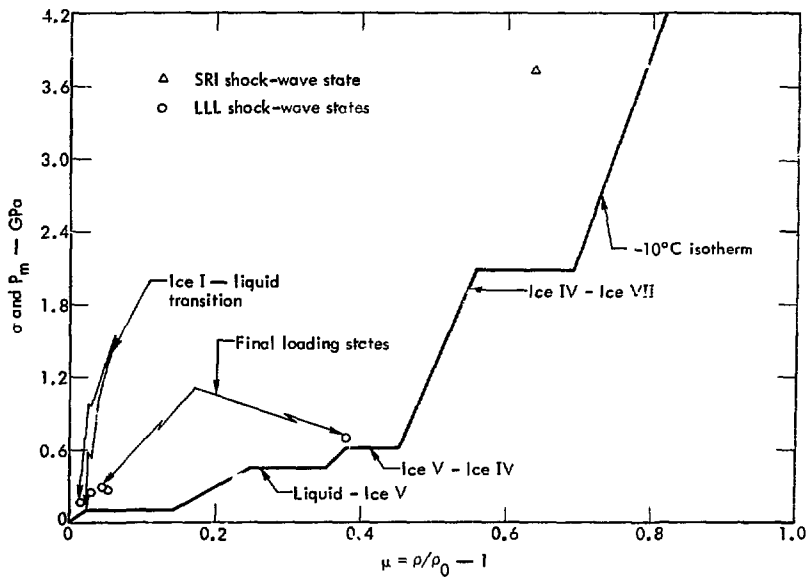

Fig. 29. A comparison of the −10°C isotherm and the Hugoniot states for polycrystalline ice.

histories with the onset of the tensile part of the wave evident for $R/R_0 > 8$. The compressive part of the wave appears to be spreading with propagation. The records at R/R_0 of 3.4 and 6.05 show evidence of rate effects cr precursor development. However, the records for $R/R_0 \geq 8$ show no such evidence which is somewhat inconsistent with gas-gun data. The decay of the peak particle velocity with radius goes as approximately $R^{-1.6}$. The value of particle-velocity and stress at $R/R_0 = 1$ (i.e., the rock-HE interface) were determined by H. C. Rodean. The details are presented in the Appendix.

<u>Westerly Granite</u>

Table 3 gives a summary of the high-explosive data obtained on Westerly granite. Typical profiles are shown in Fig. 39. These profiles show little spreading with distance. The onset of the tensile wave is shown by the stress record at $R/R_0 = 5.17$. The peak values as a function of radius are given in Figs. 40 and 41. The similarity in shape and slope of the decay of peak stress and peak particle velocity in encouraging in that it indicates a consistency between the two measurement techniques. The rate of decay of peak values in Westerly granite goes as $R^{-1.5}$. This decay rate is somewhat
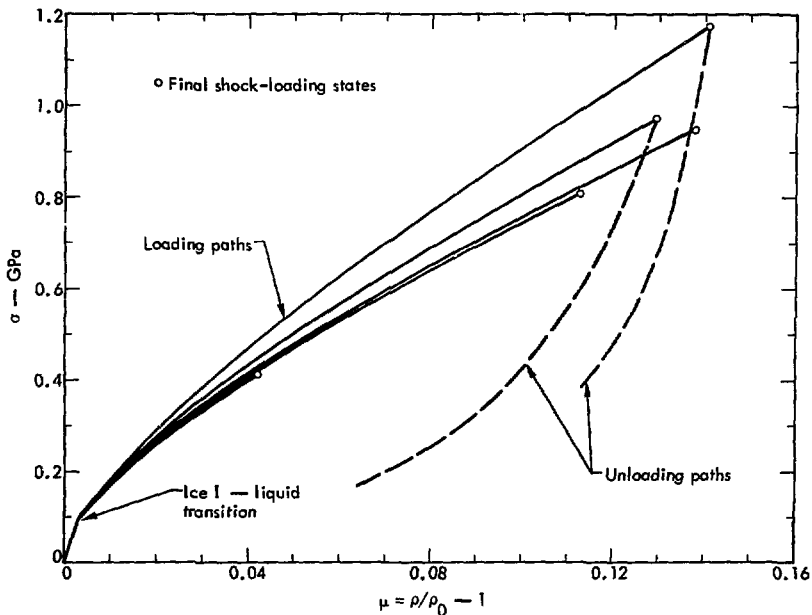

Fig. 30. Shock-loading and unloading states for water-saturated frozen West Lebanon till. The path to the Ice I — liquid trans'tion point is the average for the five experiments.
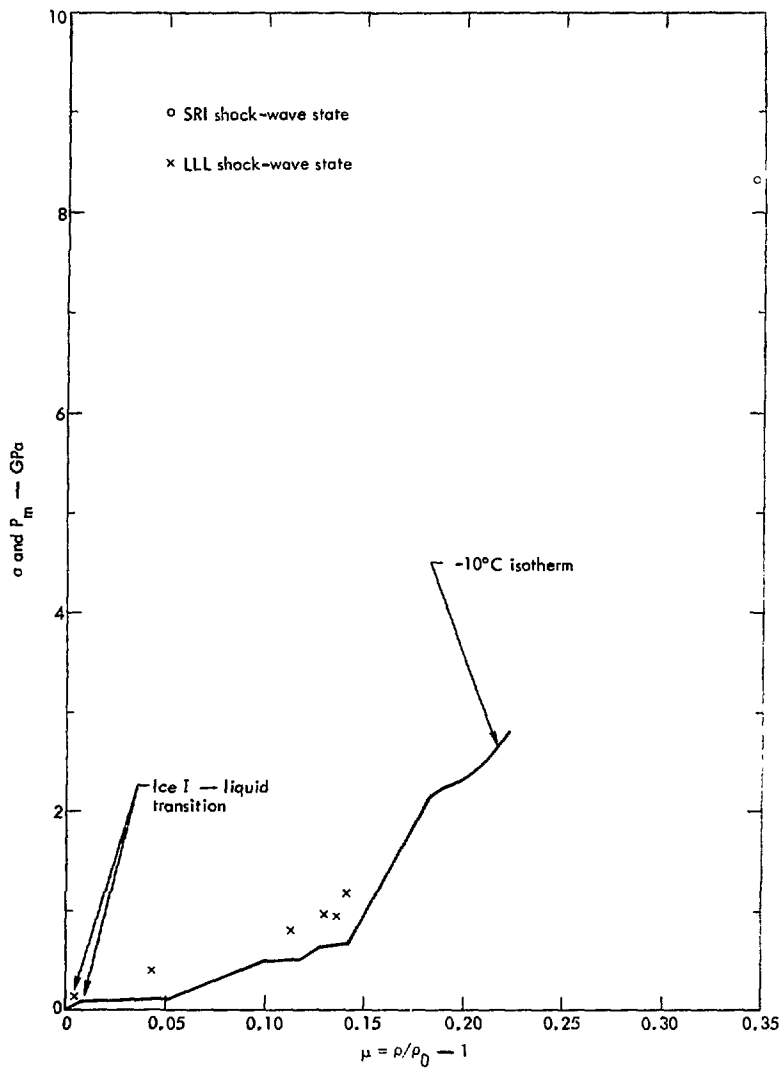
Fig. 31. A comparison of the -10°C isotherm and Hugoniot states for water-saturated frozen West Lebanon glacial till.

larger than expected, considering near-elastic behavior in the gas-gun experiments.

Nugget Sandstone

Data from the HE experiments on Nugget sandstone are given in Table 4 and in Figs. 42-44. The results at R/R_0 of 3.4 and 6.1 on two different experiments disagree. The conclusion is that a systematic error occurred in one of these experiments, and an additional experiment is planned as a check. Figure 44 shows some of the particle-velocity time histories. The loading wave shows little spreading with distance.

Polycrystalline Salt

The HE experiments on polycrystalline salt are summarized in Table 5 and

Figs. 45-47. If all of the particle-velocity data are fit with a single line the decay is as $R^{-2.0}$, but if a line is fit to the two experiments separately the decay in each is $R^{-1.8}$. A fit to the four stress points gives $R^{-1.7}$. Additional experiments will be conducted to resolve this inconsistency.

For $R/R_0 > 6$, the records show a precursor developing and for $R/R_0 > 8$, the initial part of the tensile wave is evident. The last three records (at $R/R_0 = 8.02$, 10.69 and 14.70) show a wave which appears to propagate with a constant width.

Mt. Helen Tuff

The data on dry Mt. Helen Tuff are given in Table 6 and in Figs. 48 and 49.
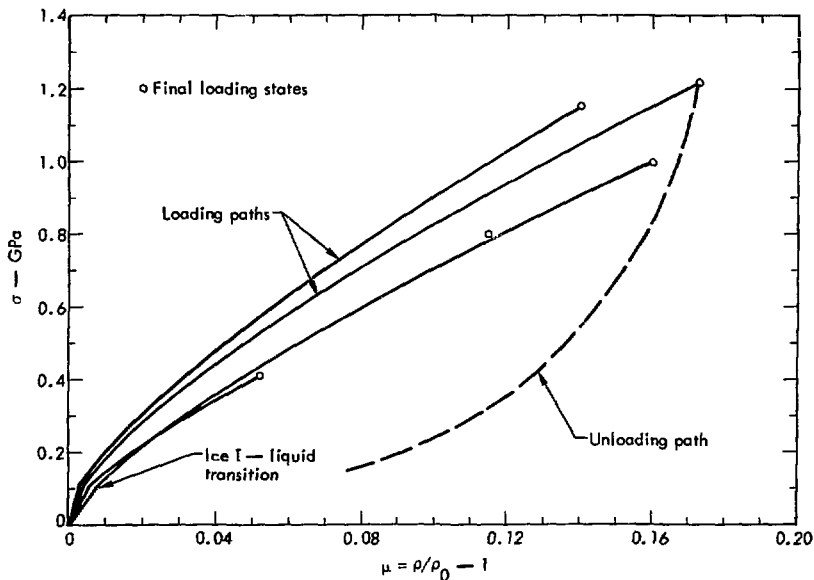
Fig. 32. Shock-wave loading and unloading states for water-saturated frozen Ottawa banding sand.
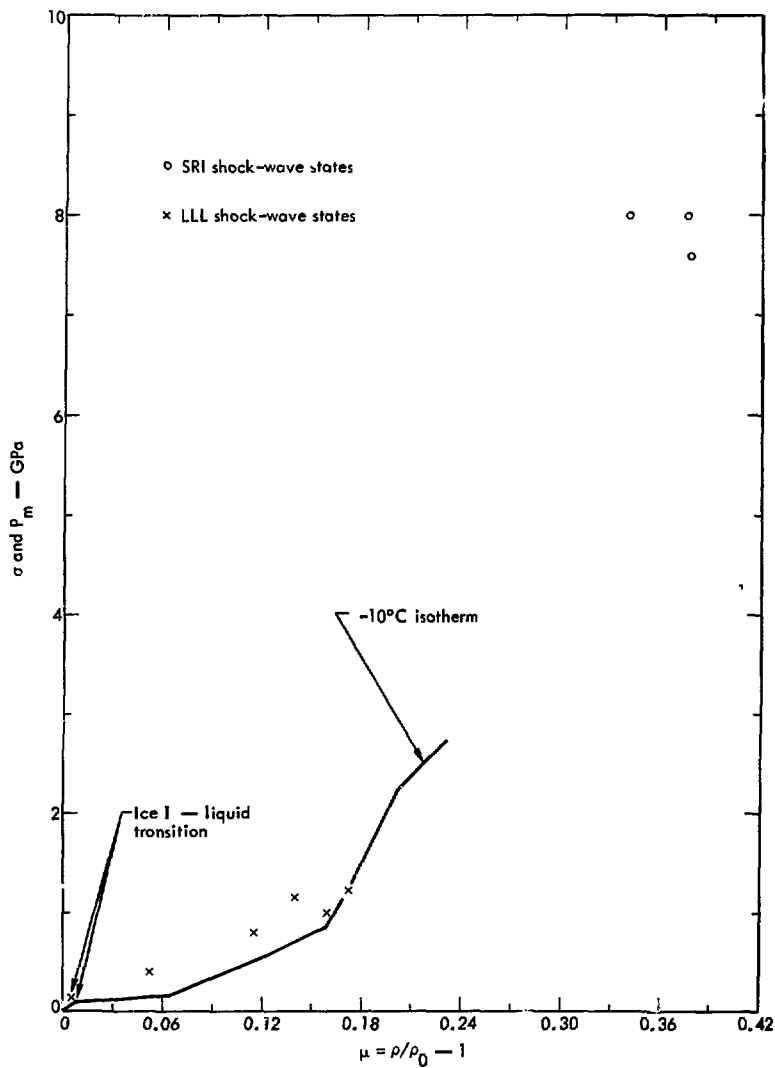
Fig. 33. A comparison of the -10°C isotherm and Hugoniot states for water-saturated frozen Ottawa banding sand.

Table 1. Peak values of particle velocity (U_p) and times of arrival (TOA) for PMMA.

Experiment number	R_0 (cm)	R/R_0	U_p (peak) (km/s)	TOA (μs)
79	1.90	2.0	0.495	6.5
79		2.0	0.555	6.4
79		3.34	0.228	14.1
79		3.34	0.232	14.3
79		5.0	0.145	24.2
79		5.0	0.141	24.4
79		6.4	0.100	33.3
79		6.4	0.103	33.4
76	0.95	10.0	0.050	25.0
72		10.0	0.053	28.7
72		10.0	0.046	26.0
72		12.7	0.044	37.4
72		12.7	0.0475	37.3
76		12.7	0.043	37.6
76		15.1	0.038	37.5
76		15.37	0.030	47.2

Fig. 34. Peak values of particle velocity for PMMA as measured in the small-scale HE experiments.
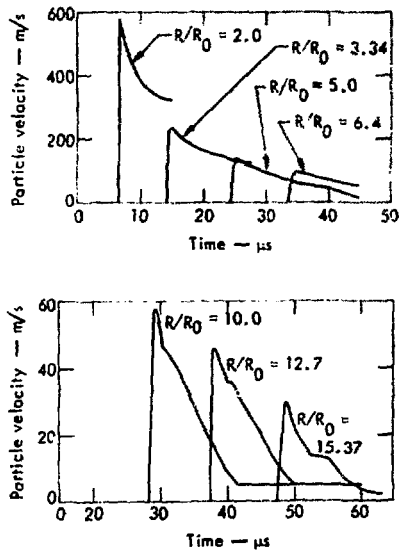
Fig. 35. Particle-velocity time profiles for PMMA.
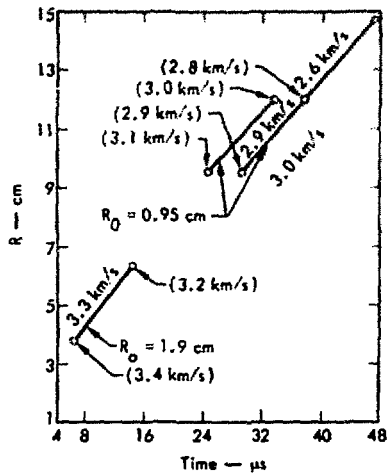
Fig. 36. Measured average shock velocities compared to values based on Barker's[13] data.

-28-

Experiment number	R_0 (cm)	R/R_0	t_p (peak) Gate at t	TOA (μs)
98	1.50	7.01	0.44 0.46	5.55
96	1.50	3.40	0.156 0.147	8.01
72	1.50	4.97	0.060	
58	1.50	4.04	0.032	14.0
73	1.50	7.44	0.065 0.042	
93	0.55	5.07	0.045 0.0505	10.4
97	0.55	10.76	0.0525 0.072	14.4
95	0.55	14.75	0.0155 0.034	20.0

Fig. 37. Peak particle velocities for the
small-scale HE experiments in
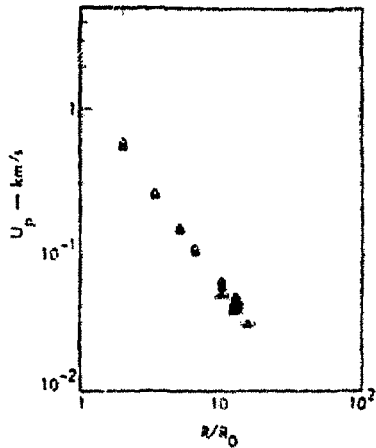Blair dolomite.

The samples in these experiments, unlike
the gas-gun samples, were not under
vacuum during the experiments. There-
fore, the average density, 1.52 Mg/m^3,
reflects the moisture picked up from the
atmosphere. Stress-time histories were
recorded on four gages, and the peak
values are shown in Fig. 48. Particle-
velocity time histories are shown in Fig.
50, and peak values are plotted as a
function of scaled distance in Fig. 49.
The apparent decay is proportional to
$R^{-2.5}$ until a stress of approximately
0.03 GPa is reached where the rate seems
to slow considerably. Below this stress
level, one would expect near-elastic
behavior of the matrix material.[19] In
Fig. 50, gages at $R/R_0 > 8$ show a neg-
ative particle velocity or a change in
direction of particle motion. This is
associated with the arrival of the tensile
part of the outgoing shock wave. Com-
parison of these waves for $R/R_0 > 8$ in-
dicate that the compressive part of
the wave spreads in time as it atten-
uates.
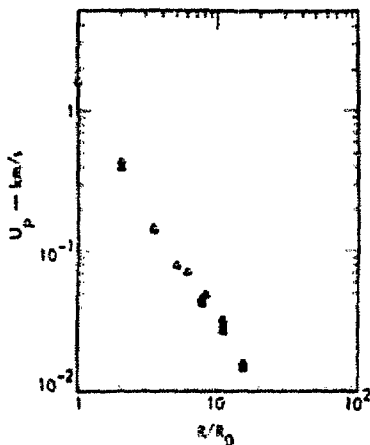
Table 7 and Figs. 48, 49 and 51 give
the data obtained on samples of saturated
Mt. Helen tuff. These samples were
vacuum-saturated and submerged in
water for the experiment. The various
plates were placed one on top of another
with water rather than epoxy used in the
interfaces. The peak particle velocity,
shown in Fig. 36, decays as $R^{-1.9}$.

Indiana Limestone

The HE experiments on Indiana lime-
stone were carried out in the same way
as for Mt. Helen tuff. Tables 8 and 9 and
Figs. 52 and 53 give the peak values for
all experiments. Representative profiles
are given in Figs. 54 and 55. These data
are similar to the Mt. Helen tuff except
for the precursor in the saturated lime-
stone shown in Fig. 55.

The dry limestone, like the dry tuff,
shows a change in rate of decay. The
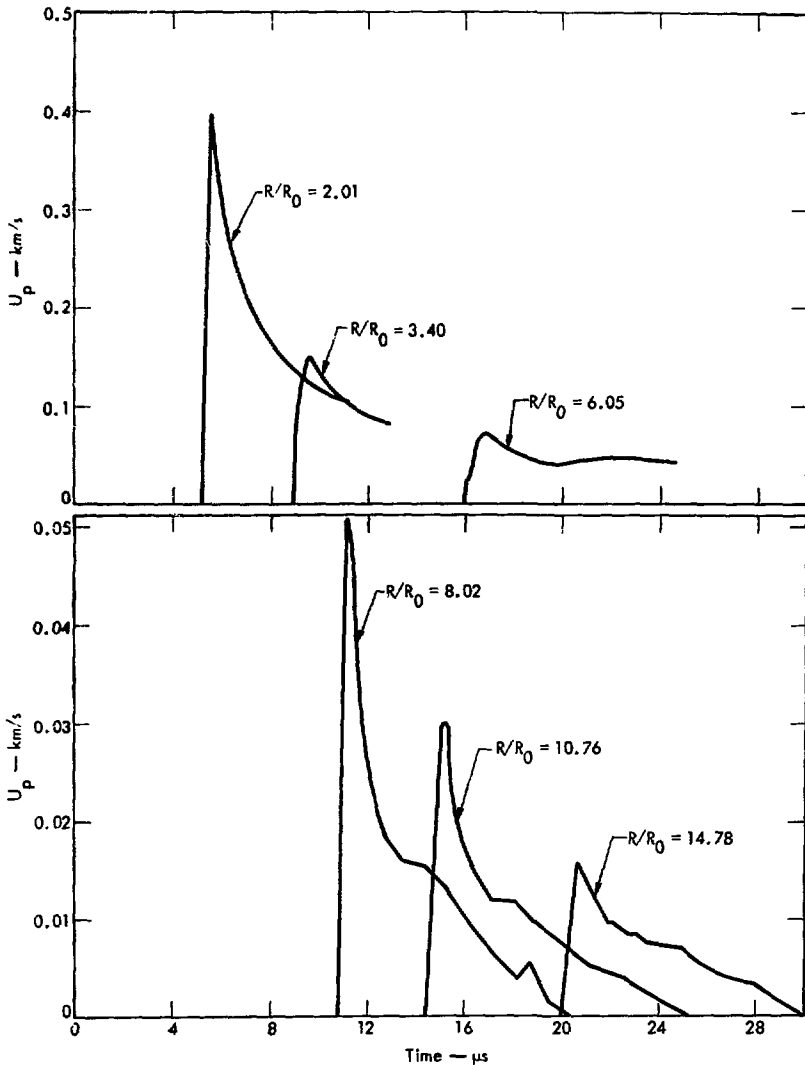
Fig. 38. Particle-velocity time profiles for Blair dolomite.
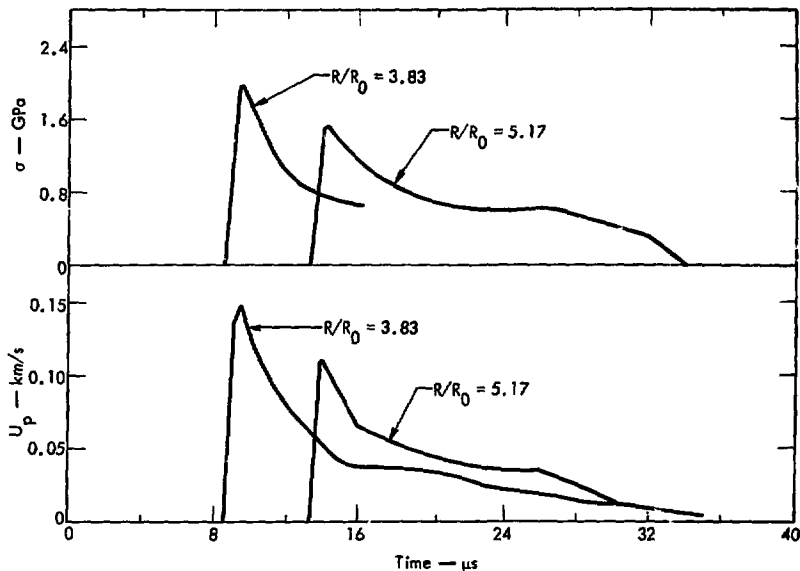
Fig. 39. Particle-velocity and stress-time histories for Westerly granite.

Table 3. Peak particle velocities and peak stresses for Westerly granite.

Experiment number	R_0 (cm)	R/R_0	U_p (peak) (km/s)	σ (peak) (GPa)
2	1.90	2.03	0.418	
4	1.90	2.03	0.454	
4	1.90	3.42	0.149	2.503
2	1.90	3.43	0.167	2.201
4	1.90	6.12	0.091	1.314
2	1.90	6.13	0.084	1.278
			0.082	
1	0.95	7.99	0.05	0.750
3	0.95	8.02		0.672
1	0.95	10.79		0.438
3	0.95	10.82	0.032	0.435
1	0.95	14.86	0.019	0.273
3	0.95	15.11	0.020	0.250
5	1.90	2.01	0.455	
5	1.90	3.03	0.213	2.62
5	1.90	3.83	0.148	1.97
5	1.90	5.17	0.110	1.53
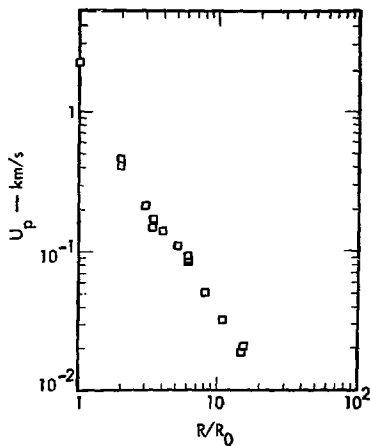
Fig. 40. Peak particle velocities for Westerly granite from the small-scale HE experiments.

initial rate is $R^{-2.4}$, but at approximately 0.1 GPa the rate changes to $R^{-1.6}$.

The saturated data appear to fit a decay law between $R^{-1.6}$ and $R^{-1.9}$, but inconsistent data at $R/R_0 \approx 8$ have made additional experiments necessary.

Frozen Materials

The data from the HE experiments on polycrystalline ice and the two frozen soils are given in Tables 10-12 and Figs.

Fig. 41. Peak stresses for Westerly granite from the small-scale HE experiments.

Table 4. Peak particle velocities, peak stresses, and times of arrival for Nugget sandstone.

Experiment number	R_0 (cm)	R/R_0	U_p (peak) (km/s)	σ peak (GPa)	TOA (μs)
116	1.90	2.04	0.431		3.66
116	1.90	3.41	0.202	2.16	8.96
118	1.90	6.12	0.086 0.088	1.05	19.08
106	1.90	3.45	0.160 0.153		3.67
106	1.90	6.13	0.069	0.91	14.72
107	0.95	8.03	0.046		7.17
107	0.95	10.81	0.0275	0.36	13.45
107	0.95	14.87	0.0144	0.17	23.30

Fig. 42. Peak particle velocities for Nugget sandstone from the small-scale HE experiments.
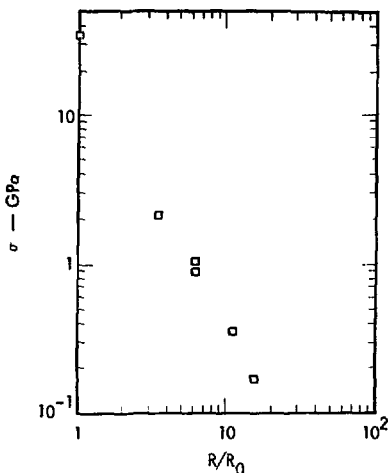
Fig. 43. Peak stresses for Nugget sandstone from the small-scale HE experiments.
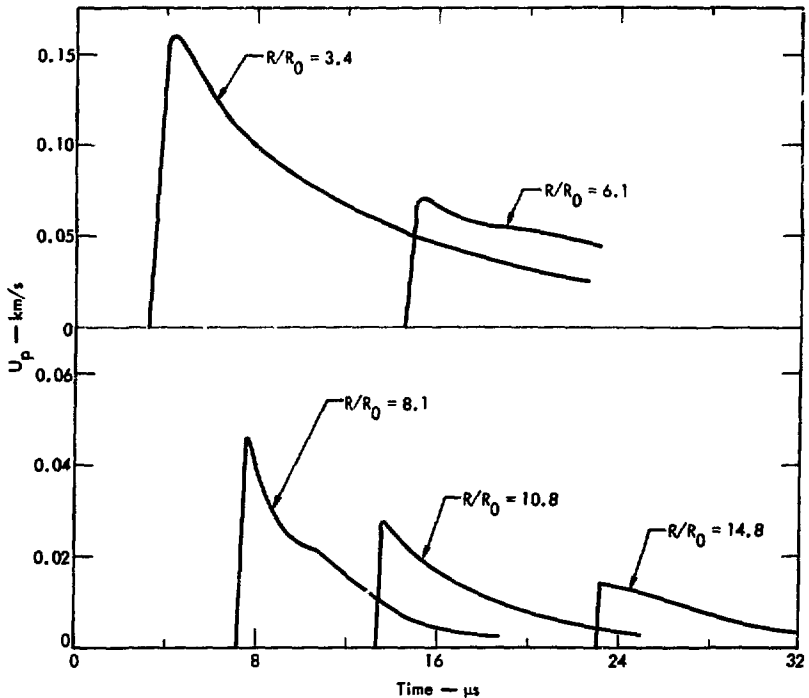
Fig. 44. Particle-velocity time histories for Nugget sandstone.

56-59. Figure 56 compares the peak particle velocity at various scaled radii

Table 5. Peak particle velocities, peak stresses, and times of arrival for polycrystalline salt.

Experiment number	R_0 (cm)	R/R_0	U_p (peak) (km/s)	σ (peak) (GPa)	TOA (μs)
116	1.90	2.03	0.608		3.37
		3.36	0.254	1.839	8.20
		6.06	0.0845		20.10
		8.06	0.0815		19.95
117	0.95	8.02	0.0365 0.0373	0.352	18.25
		10.69	0.0208 0.0204	0.210	25.35
		14.70	0.0116 0.0113	0.156	33.35

while Figs. 57-59 give typical particle-velocity time histories at various points within the material. These experiments were conducted at -10 ± 2°C.

From Fig. 56, the soils indicate a decay rate as $R^{-2.0}$. However, poly-crystalline ice decays as $R^{-1.6}$. This difference is at first glance unexpected, in view of the similar loading and un-loading behavior in the gas-gun experi-ments. However, Figs. 57, 58 and 59 all clearly show the precursor-wave and main-wave broadening attributed to phase transformation kinetics. A

-33-
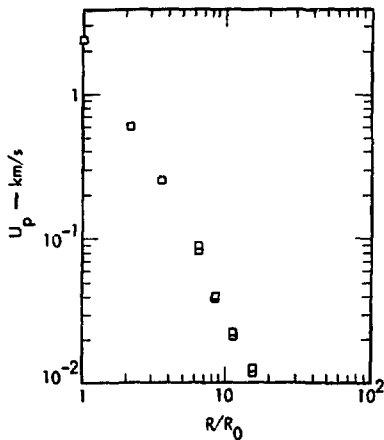
Fig. 45. Peak particle velocities for salt from small-scale HE experiments.

Fig. 46. Peak stresses in polycrystalline salt from small-scale HE experiments.

comparison of ice and soil profiles shows the soil waves to be much broader. This broadening appears to occur in both the loading and unloading parts of the waves. Undoubtedly, this greater broad-ening is due to the two-component system which affects the flow through dispersion and through altering the kinetics of the phase transformation.

-34-
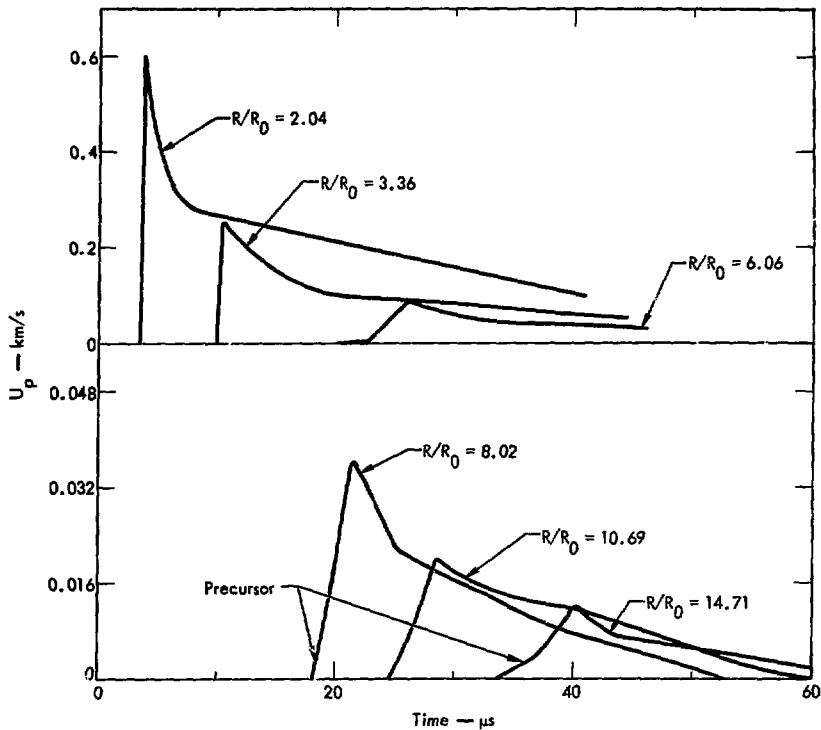
Fig. 47. Particle-velocity time profiles for polycrystalline salt.

Table 6.	Peak particle velocities, peak stresses, and times of arrival for the small-scale HE experiments on dry Mt. Helen tuff.				
Experiment number	R_0 (cm)	R/R_0	U_p (peak) (km/s)	σ (peak) (GPa)	TOA (μs)
84	1.90	2.00	0.405	0.93	8.75
84	1.90	3.31	0.132	0.365	18.00
75	1.90	4.57	0.050		29.00
75	1.90	5.94	0.025		38.00
84	1.90	5.98	0.0285		37.00
85	0.95	8.21	0.0132		28.00
85	0.95	10.94	0.0083	0.022	38.0
85	0.95	14.87	0.0063	0.016	52.0

Table 7.	Peak particle velocities, peak stresses, and times of arrival in small-scale HE experiments on saturated Mt. Helen tuff.			
Experiment number	R/R_0	U_p (peak) (km/s)	σ (peak) (GPa)	TOA (μs)
1.90	2.04	0.527		5.2
1.90	3.39	0.195	0.70	14.4
1.90	6.07	0.065	0.250	35.6
0.95	8.06	0.0294		19.9
0.95	8.06	0.0284		19.8
0.95	10.80	0.022		30.1
0.95	10.80	0.020		29.8
0.95	14.85	0.014		45.0
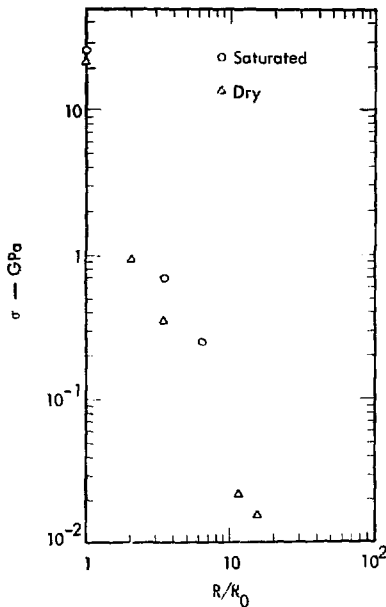
Fig. 48. Peak stresses from the small-scale experiments in Mt. Helen tuff.
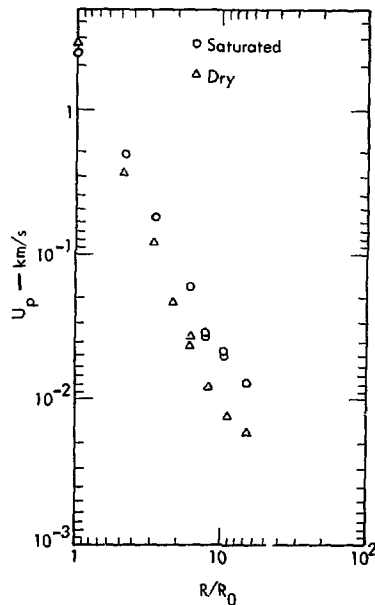
Fig. 49. Peak particle velocities from the small-scale HE experiments in Mt. Helen tuff.
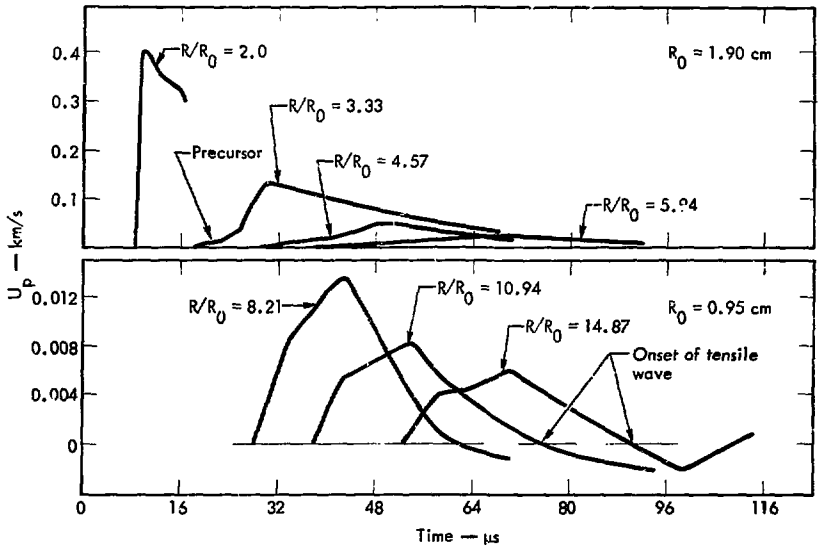
Fig. 50. Particle-velocity time histories in dry Mt. Helen tuff.
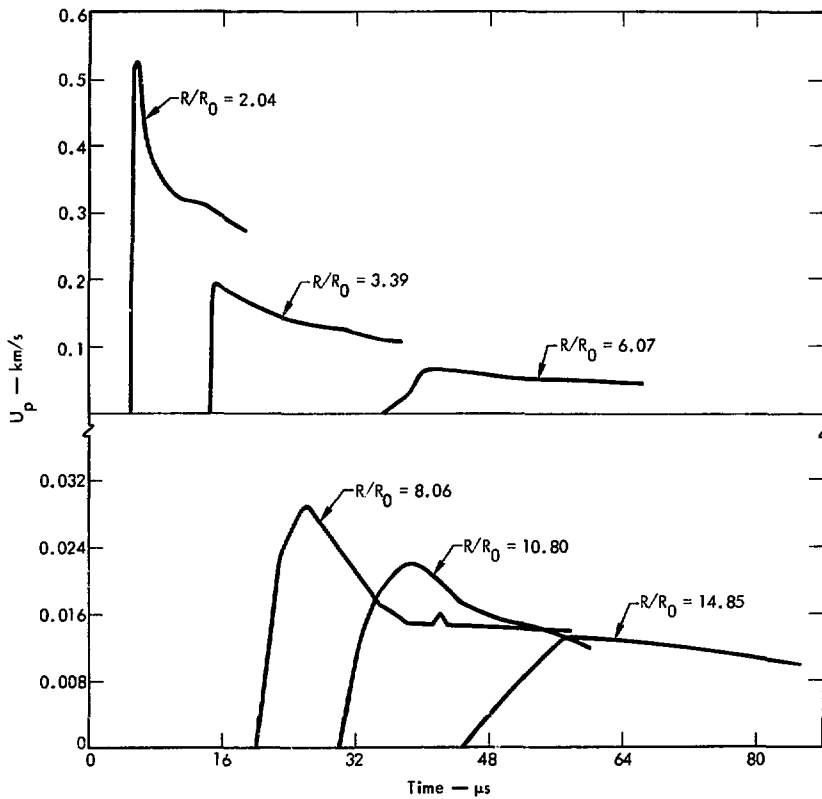
Fig. 51. Particle-velocity time histories in saturated Mt. Helen tuff.

Table 8. Peak particle velocities, peak stresses, and times of arrival for dry Indiana limestone.

Experiment number	R_0 (cm)	R/R_0	U_p (peak) (km/s)	σ (peak) (GPa)	TOA (μs)
102	1.90	2.02	0.283		3.76
			0.297		
		3.39	0.106		10.00
			0.104		
		6.07	0.022		19.51
			0.023		
103	0.95	8.02	0.011	0.100	12.28
		10.82	0.0069	0.059	18.15
		14.87	0.0041	0.036	26.44

Table 9. Peak particle velocities, peak stresses, and times of arrival for saturated Indiana limestone.

Experiment number	R_0 (cm)	R/R_0	U_p (peak) (km/s)	σ (peak) (GPa)
113	1.90	2.01	0.406	
104	1.90	2.03	0.387	
			0.378	
113	1.90	3.38	0.165	
104	1.90	3.40	0.160	
			0.160	
113	1.90	6.07	0.052	0.350
			0.051	
104	1.90	6.07		0.280
105	0.95	8.03	0.016(?)	0.153
114	0.95	8.03	0.018	0.183
105	0.95	10.77	0.0115	0.126
114	0.95	10.74	0.0138	
105	0.95	14.83	0.0090	
114	0.95	14.79	0.0098	
			0.0082	

Fig. 52. Peak stresses from small-scale HE experiments on Indiana limestone.
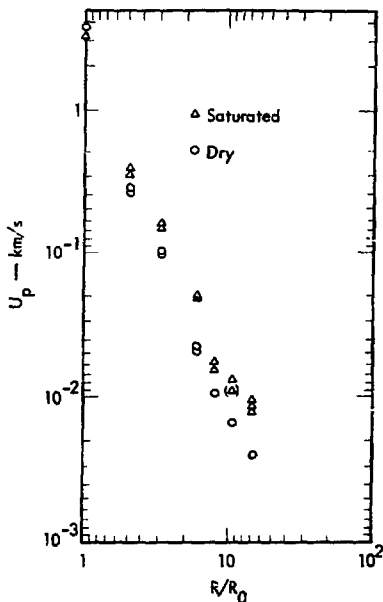
Fig. 53. Peak particle velocities from small-scale HE experiments on Indiana limestone.
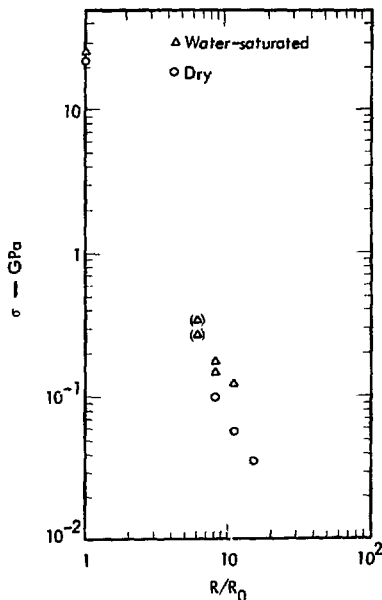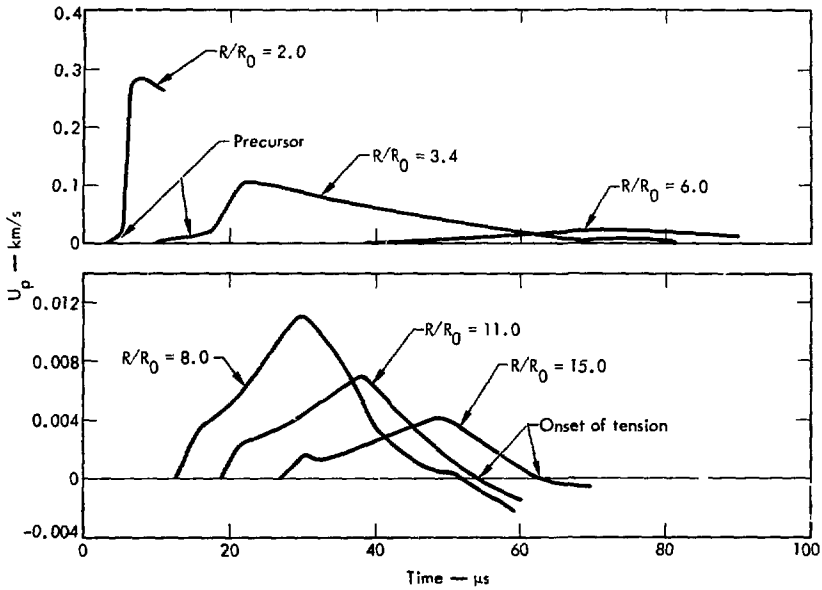
Fig. 54. Particle-velocity time histories for dry Indiana limestone.
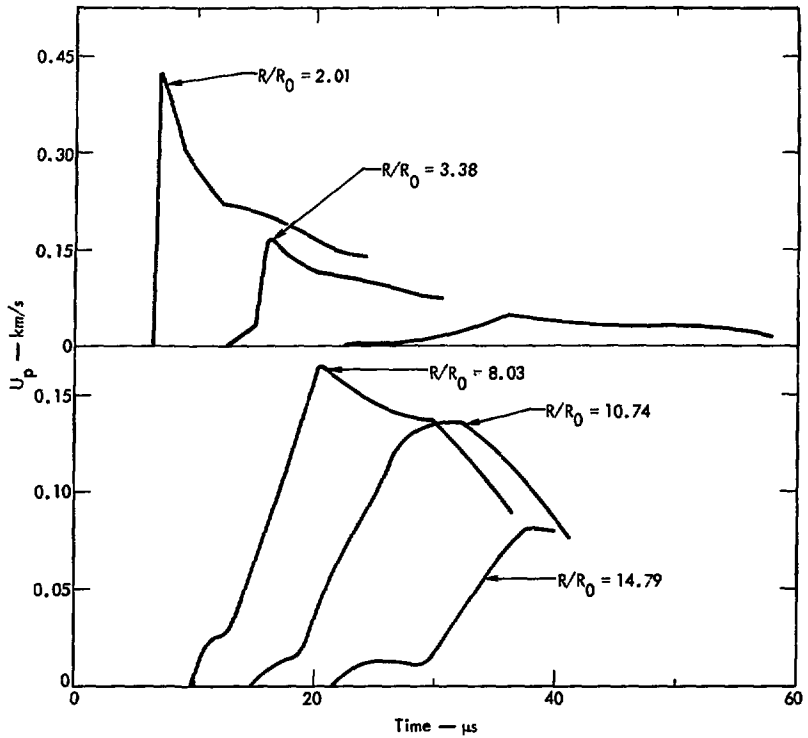
Fig. 55. Particle-velocity time histories for saturated Indiana limestone.

Table 10. Peak particle velocity for the small-scale HE experiments in polycrystalline ice.

Experiment number	R_0 (cm)	R/R_0	U_p (peak) (km/s)
87	1.90	2.05	0.583
			0.582
71	1.90	2.65	0.22
			0.21
87	1.90	3.39	0.226
			0.231
74	1.90	3.63	2 peaks 0.335 0.37
74	1.90	5.26	0.12
			0.11
87	1.90	6.04	0.104
			0.103
88	0.95	8.06	0.062
			0.062
	0.95	10.59	0.040
			0.040
	0.95	14.44	0.026
			0.027

Table 11. Peak particle velocities for the small-scale experiments in frozen Ottawa banding sand.

Experiment number	R_0 (cm)	R/R_0	U_p (peak) (km/s)
78	1.90	4.02	0.109
			0.111
80	1.90	4.02	0.117
			0.108
78	1.90	5.40	0.066
			0.066
80	1.90	5.40	0.068
			0.066

Table 12. Peak particle velocities from the small-scale HE experiments on frozen West Lebanon glacial till.

Experiment number	R_0 (cm)	R/R_0	U_p (peak) (km/s)
83	1.90	3.41	1.61
			1.61
83	1.90	4.82	0.080
			0.078
81	0.95	8.07	0.027
81	0.95	10.92	0.016
			0.014
81	0.95	13.73	0.0088
			0.0077

Fig. 56. Peak particle velocities for the frozen materials.

Fig. 57. Particle-velocity time histories in polycrystalline ice.
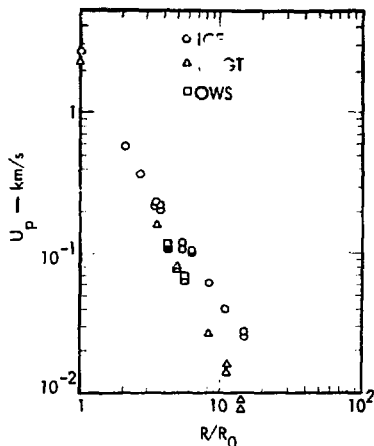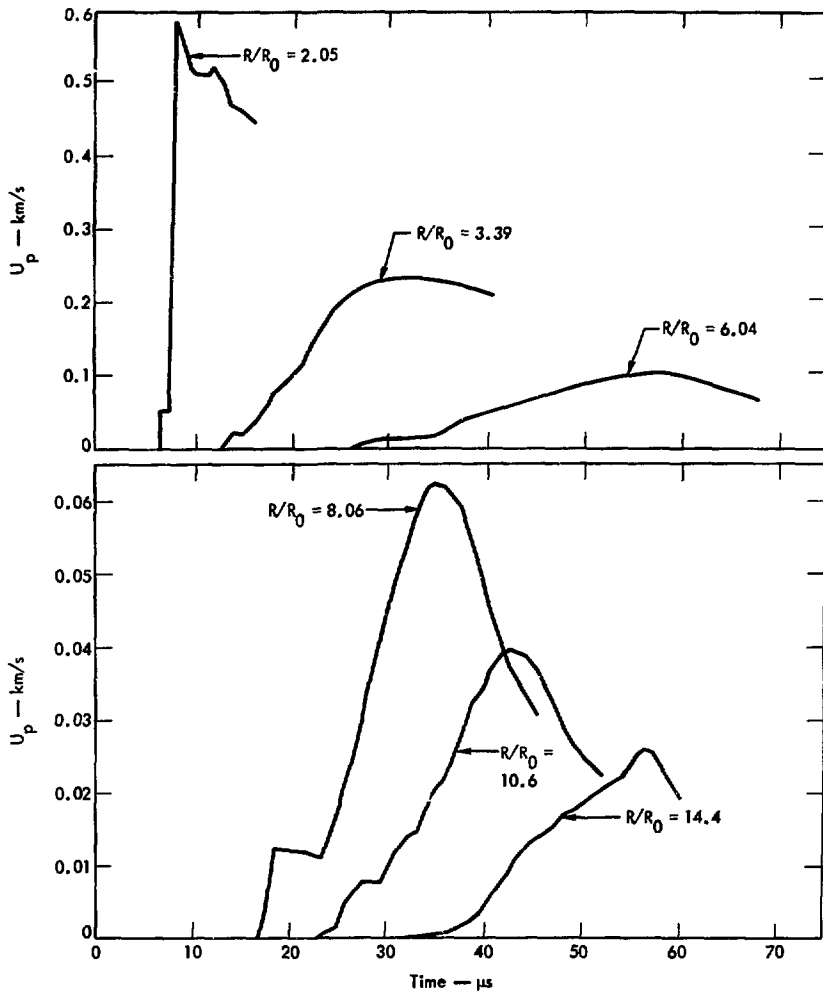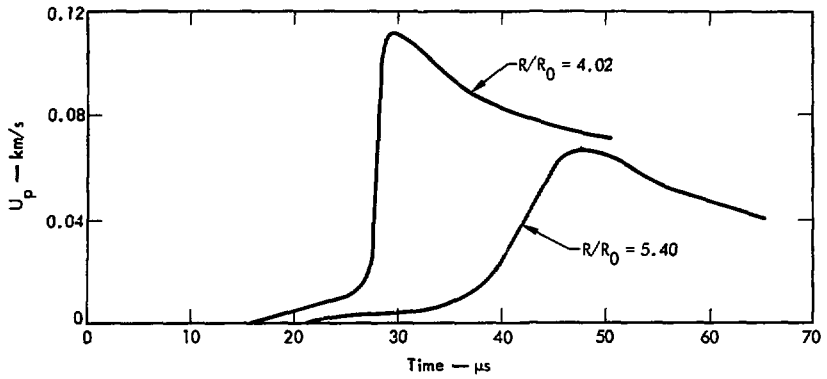
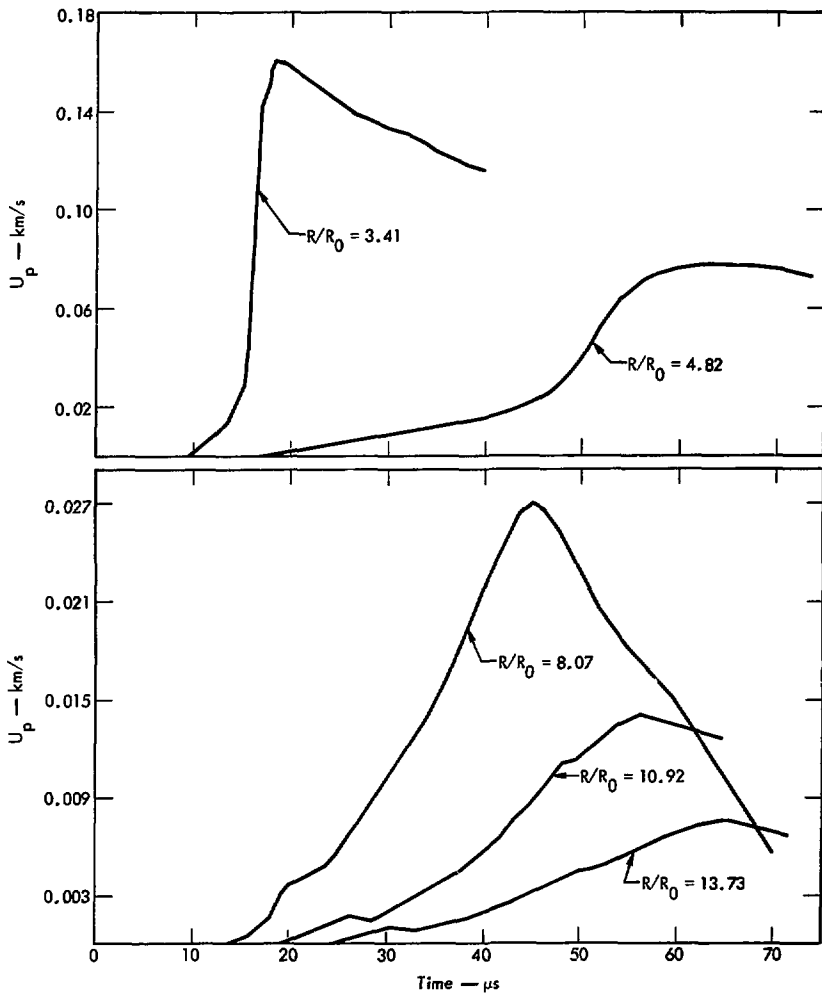Fig. 58. Particle-velocity time histories in frozen Ottawa banding sand.

Fig. 59. Particle-velocity time histories in frozen West Lebanon glacial till.

V. Conclusions

The details of relative coupling will have to wait upon constitutive model development and calculation. However, a number of preliminary conclusions can be drawn through comparison of data for the various materials.

All of the dynamic data on PMMA — acoustic, gas-gun and spherical HE — appear to be consistent. This agreement for the test material provides the desired confidence in the techniques. The apparent limiting decay (i. e., $R^{-1.25}$) is considerably higher than the expected R^{-1} for a spherical steady elastic wave in the farfield. However, the data only extends to approximately 0.1 GPa. This, coupled with the visco-elastic behavior of PMMA, make the observed decay reasonable.

The gas-gun data indicate that the Nugget sandstone and Westerly granite behave to a first approximation as simple elastic solids. In the HE experiments, the loading wave shows no apparent dispersion and the entire compressive part of the wave appears to be steady. However, the relatively high decay rate, $R^{-1.5}$, suggests dispersion perhaps due to microcracks and non-elastic matrix material, and may represent a lower limit for rocks.

Blair dolomite, although about the same porosity as Westerly granite and only one-third the porosity of Nugget sandstone, acts quite differently. The wave profiles are dispersive and show strain-rate sensitivity. Whether this behavior is associated with porosity or some other material property is not completely clear, but it appears that the weaker cementing inherent in carbonate rocks may account for this behavior. When considering field experience,[6] the decay rate of peak particle velocity as $R^{-1.6}$ is less than expected when compared to granite. However, since dolomite seems to lose porosity at lower stress levels, a small increase in porosity in the field situation could cause a significant increase in decay rate.

Although the study of polycrystalline salt is incomplete, the gas-gun results indicate elimination of porosity at low stress levels. This elimination of porosity would attenuate the shock wave in the HE experiments and explain a decay rate of $R^{-1.8}$. In a salt dome with low porosities, a completely different decay law would be expected.

The behavior of the two dry porous materials, Mt. Helen tuff and Indiana limestone, in the HE experiments is similar. Both decay as approximately $R^{-2.5}$ until a stress equivalent to matrix failure is reached. The data beyond this radius suggest a rate of $R^{-1.5}$ to $R^{-1.6}$. The rapid decay at the higher stresses is associated with the irreversible compaction of pores. This strain-rate-sensitive process also accounts for the non-steady waves seen in the radial flow. The spreading of the waves at larger R/R_0 is probably associated with non-elastic grain boundaries or microcracks.

An examination of all these data on dry rock suggests a limiting or elastic decay rate for rocks of $R^{-1.5}$. This relatively high rate is somewhat surprising, but in all cases is probably associated with dispersion due to microcracks and/or

plastic yielding within grain boundaries. These data also suggest that the strength of the matrix (i.e., the strength of cementing) is an extremely important parameter in determining relative coupling in porous materials. This is most dramatically illustrated in the comparison of gas-gun data on the Nugget and Wagon Wheel sandstones.

Porous materials saturated with water behaved similarly in the HE experiments with both showing peak particle-velocity decay as $R^{-1.9}$. This rate in saturated rocks indicates a strong attenuation due to two-component interactions. These data also suggest that, since rocks lose most of their strength once saturated, saturated rocks lose their dependence on two key parameters, strength and porosity.

The frozen materials provide an extremely interesting special case. Ice, which is very weak, would be expected to couple like water except for the ice-water phase transformation at approximately 0.1 GPa. Strain-rate effects apparently associated with this transformation cause a large hysteresis loop in the loading-unloading cycle which in turn causes a decay in peak particle velocity proportional to $R^{-2.0}$. This would suggest that frozen saturated soils are somewhat weaker couplers than saturated soils, and also suggests that partially saturated frozen soils may be even weaker couplers.

When all these results are considered together, they suggest that porosity and material strength, especially the cementing of the matrix, are closely tied in determining the effective elastic radius for a spherical source and thus the relative coupling. They suggest that two-component interaction plays an important role in attenuation of peak values and in the shape of wave profiles. They also suggest the importance of phase transformations, microcracks and grain boundary effects in establishing a proper coupling model.

Acknowledgments

References

1. M. L. Wilkins, *Lawrence livermore* Laboratory, Rept. UCRL-7322, Rev. 1 (1969).

2. J. T. Cherry and F. L. Petersen, Proceedings of the Topical Meeting on Engineering with Nuclear Explosives (American Nuclear Society, Hinsdale, Ill., 1970).

3. J. T. Cherry, S. Sack, G. Maenchen and V. Kransky, Lawrence Livermore Laboratory, Rept. UCRL-50987 (1970).

4. J. F. Schatz, Lawrence Livermore Laboratory, Rept. UCRL-51689 (1974).

5. D. E. Burton and J. F. Schatz, Lawrence Livermore Laboratory, Rept. UCID-16719, in preparation (1975).

6. H. C. Rodean, Nuclear Explosion Seismology (USAEC Division of Technical Information Extension, Oak Ridge, Tennessee, 1971).

7. D. D. Keough, SRI, Palo Alto, Calif., Rept. for Project PGU-7511 (1969).

8. M. J. Ginsberg, Effects of Stress on the Electrical Resistance of Ytterbium and Calibration of Ytterbium Stress Transducers, Contract DNA 001-72-C-0146, SRI Project PYU-1979 (1974).

9. S. J. Spataro, Lawrence Livermore Laboratory, Internal Document UOPKK 72-27 (1972). Readers outside the Laboratory who desire further information on LLL internal documents should address their inquiries to the Technical Information Department, Lawrence Livermore Laboratory, Livermore, CA 94550.

10. R. Fowles and R. F. Williams, J. Appl. Phys. 41, 360 (1970).

11. M. Cowperthwaite and R. F. Williams, J. Appl. Phys. 42, 456 (1971).

12. K. W. Schuler and J. W. Nunziato, Sandia Labs., Albuquerque, N. Mex., Rept. SC-DC-721174 (1972).

13. L. M. Barker and R. E. Hollenback, J. Appl. Phys. 41, 4208 (1970).

14. D. R. Stephens, H. C. Heard and R. N. Schock, Lawrence Livermore Laboratory, Rept. UCID-16007 (1972).

15. I. Y. Borg, Lawrence Livermore Laboratory, Internal Rept. UOPKK 72-40 (1972).

16. H. C. Heard, A. Duba, A. E. Abey and R. N. Schock, Lawrence Livermore Laboratory, Rept. UCRL-51465 (1973).

17. H. C. Heard, A. E. Abey, B. P. Bonner, R. N. Schock, Lawrence Livermore Laboratory, Rept. UCRL-51642 (1974).

18. R. N. Schock, A. E. Abey, B. P. Bonner, A. Duba and H. C. Heard, Lawrence Livermore Laboratory, Rept. UCRL-51447 (1974).

19. H. C. Heard, B. P. Bonner, A. G. Duba, R. N. Schock and D. R. Stephens, Lawrence Livermore Laboratory, Rept. UCID-16261 (1973).

20. D. E. Grady and W. J. Murri, Stanford Research Institute, Palo Alto, Cal., Interim Tech. Rept. PYU-1803 (1973).

21. H. C. Heard, A. E. Abey and B. P. Bonner, Lawrence Livermore Laboratory, Rept. UCID-16501 (1974).

22. E. Chamberlain and P. Hockstra, U. S. Army Cold Regions Research and Engineering Laboratory Technical Rept. 225 (1970).

23. D. B. Larson, G. D. Bearson and T. R. Taylor, North American Contribution, Second Intern. Conf. of Permafrost, National Academy of Science, Washington, D. C., 1973.

24. W. J. Murri and C. W. Smith. Stanford Research Institute, Palo Alto, Cal., Interim Tech. Rept. PGU-6618 (1970).

25. J. R. Hearst, Lawrence Livermore Laboratory, Rept. UCID-16491 (1974).

Appendix

Conditions at the HE-Test Material Interface

No measurements were made at the interface between the high-explosive and the test material, but it is possible to calculate values for the peak radial stress and peak particle velocity at this location. There is generally an impedance mismatch between the detonating HE and the test material so the detonation wave parameter of radial stress and particle velocity are usually modified at the interface. A shock wave is always transmitted into the test material, but the stress wave reflected into the HE may be either a shock or a rarefaction wave. The solution of this problem is outlined in two books,[A-1, A-2] and is presented in more detail in two papers.[A-3, A-4]

The equations for mass and momentum conservation across the detonation wave in the HE are

$$\rho_{x0} D_{x1} = \rho_{x1} (D_{x1} - U_{x1}) , \tag{A-1}$$

$$\rho_{x0} D_{x1} U_{x1} \quad P_{x1} - P_0 . \tag{A-2}$$

The relations for the conditions immediately behind the detonation wave are

$$D_{x1} = U_{x1} + C_{x1} , \tag{A-3}$$

$$\rho_{x1} C_{x1}^2 = \overset{+}{\gamma}_{x1} P_{x1} , \tag{A-4}$$

where $\overset{+}{\gamma}$ is the effective sentropic exponent[A-5]

$$\overset{+}{\gamma} = (\partial \ln P / \partial \ln \rho)_s = (\partial H / \partial E)_s . \tag{A-5}$$

From Eqs. (A-1)-(A-4) with $P_{x1} \gg P_0$,

$$C_{x1} = \overset{+}{\gamma}_{x1} U_{x1} . \tag{A-6}$$

The mass and momentum conservation equations for the shock wave transmitted into the test material are[A-]

$$\rho_{m0} D_{m1} = \rho_{m1} (D_{m1} - U_{m1})_1 \tag{A-7}$$

$$\rho_{m0} D_{m1} U_{n\,1} = P_{m1} - P_0 . \tag{A-8}$$

The boundary conditions for the transmitted shock wave in the test material and the reflected wave in the HE are

$$U_{xz} = U_{m1} , \tag{A-9}$$

$$P_{xz} = P_{m1} . \tag{A-10}$$

Assuming a shock wave is reflected into the HE, the equations for conservation of mass and momentum are[A-3,A-4]

$$\rho_{x1}(D_{x2} + U_{x1}) = \rho_{x2}(D_{x2} + U_{x2}) \, , \tag{A-11}$$

$$\rho_{x1}(D_{x2} + U_{x1})(U_{x1} - U_{x2}) = P_{x2} - P_{x1} \, . \tag{A-12}$$

It follows from Eqs. (A-2), (A-8)-(A-10) and (A-12) that $P_{m1} > P_{x1}$ if $\rho_{m0}D_{m1} > \rho_{x0}D_{x1}$. From the definition of the ratio of the enthalpy change to the internal energy change across a shock wave,[A-6]

$$\overset{*}{\gamma} = (H_{x2} - H_{x1})/(E_{x2} - E_{x1}) \tag{A-13}$$

and the Hugoniot relations for enthalpy and internal energy, the following relation may be derived:

$$\frac{P_{x2}}{P_{x1}} = \frac{\dfrac{\rho_{x2}}{\rho_{x1}} - \dfrac{\overset{*}{\gamma} - 1}{\overset{*}{\gamma} + 1}}{1 - \dfrac{\rho_{x2}}{\rho_{x1}}\left(\dfrac{\overset{*}{\gamma} - 1}{\overset{*}{\gamma} + 1}\right)} \, . \tag{A-14}$$

The following relation is obtained from Eqs. (A-11), (A-12) and (A-14)[A-4]:

$$\left(\frac{P_{xz}}{P_{x1}}\right)^2 - \frac{P_{xz}}{P_{x1}}\left[2 + \left(\frac{\overset{*}{\gamma} + 1}{2}\right)\left(\frac{\rho_{x1}U_{x1}}{P_{x1}}\right)^2\left(1 - \frac{U_{x2}}{U_{x1}}\right)^2\right] + 1 - \left(\frac{\overset{*}{\gamma} - 1}{2}\right)\left(\frac{\rho_{x1}U_{x1}}{P_{x1}}\right)\left(1 - \frac{U_{x2}}{U_{x1}}\right) = 0 \tag{A-15}$$

For a rarefaction wave reflected into the high explosive,[A-3,A-4]

$$U_{xz} - U_{x1} = \int_{\rho_{x2}}^{\rho_{x1}} C_x d\rho_x/\rho_x \tag{A-16}$$

and

$$P_x/P_{x1} = (\rho_x/\rho_{x1})^{*} \tag{A-17}$$

which is the integral of Eq. (A-5) assuming $\overset{*}{\gamma}$ is constant. Equations (A-4), (A-6), (A-16) and (A-17) are combined to give

$$\frac{U_{xz}}{U_{x1}} = 1 + \frac{2\overset{*}{\gamma}}{\overset{+}{\gamma} - 1}\left[1 - \left(\frac{P_{xz}}{P_{x1}}\right)^{\frac{\overset{+}{\gamma} - 1}{2\overset{+}{\gamma}}}\right] . \tag{A-18}$$

It follows from Eqs. (A-2), (A-8)-(A-10) and (A-18) that $P_{x1} > P_{x2}$ if $\rho_{x0}D_{x1} > \rho_{m0}D_{m1}$.

From Eqs. (A-2), A-8) and the linear relation between shock and particle velocities in condensed materials,[A-1,A-2]

$$D = a + bU \, , \tag{A-19}$$

the following is obtained:

$$\frac{P_{m1}}{P_{x1}} \approx \frac{P_{m1} - P_0}{P_{x1} - P_0} = b \frac{\rho_{m0}}{\rho_{x0}} \frac{U_{x1}}{D_{x1}} \frac{U_{m1}}{U_{x1}} \frac{a}{bU_{x1}} + \frac{U_{m1}}{U_{x1}}. \tag{A-20}$$

Equations (A-15) and (A-18) define the reflected shock and reflected rarefaction wave conditions, respectively, on the HE side of the interface. The transmitted shock-wave conditions on the test material side of the interface are defined by Eq. (A-20). The intersection of the curve defined by Eq. (A-20) with either the curve defined by Eq. (A-15) or that by Eq. (A-18) gives the desired solution. The solutions for the test materials which are illustrated in Fig. A-1 and listed in Table A-3 were obtained by means of these three equations and the data given in Tables A-1 and A-2.
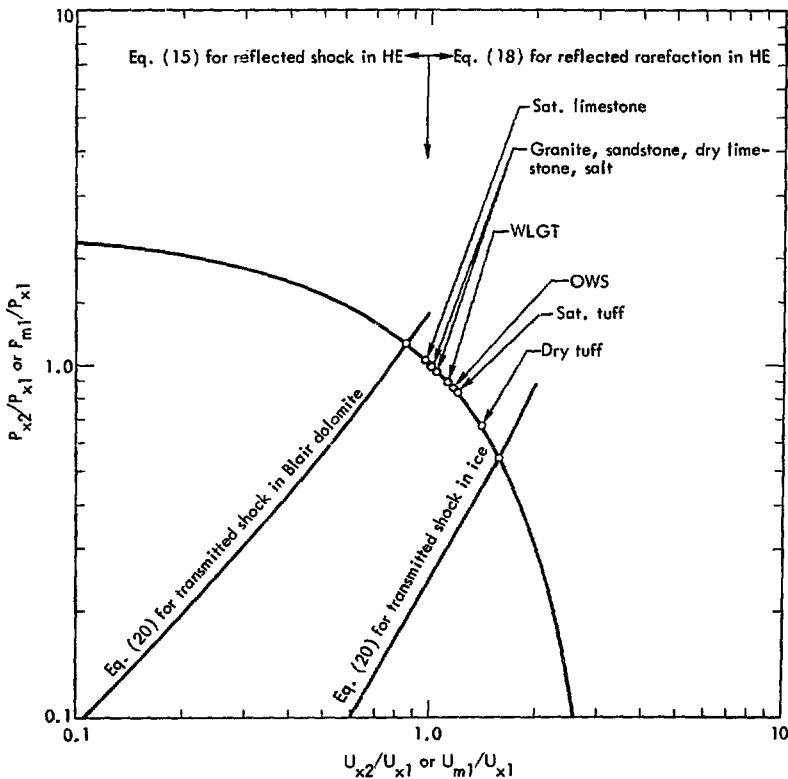

Fig. A-1. Solutions for HE-test interface conditions.

Table A-1. Properties of the explosive LX-04.

From Ref. A-7: $\rho_{x0} = 1.86$ Mg/m^3
                  $D_{x1} = 8.46$ km/s
                  $P_{x1} = 33$ GPa (calculated) and 35 GPa (measured)
                  $\stackrel{+}{\gamma}_{x1} = 2.936$
From Eq. (A-2) with $P_{x1} \gg P_0$ and using $P_{x1} = \frac{1}{2}(3.3 + 3.5) 10$ GPa:
                  $U_{x1} = 2.16$ km/s
From Eq. (A-1): $\rho_{x1} = 2.5$ Mg/m^3
From Eq. (A-3): $C_{x1} = 6.30$ km/s
From Eq. (A-4): $\stackrel{+}{\gamma}_{x1} = 2.918$, which is approximately equal to the value given in
                  Ref. A-7.

Table A-2. Properties of test materials.

Material	ρ_{m0} (Mg/m^3)	a (km/s)	b
Ice	0.917	0.85	1.55
West Lebanon glacial till	2.10	2.32	1.50
Ottawa banding sand	2.00	2.43	1.31
Salt	2.13	3.43	1.44
Westerly granite	2.65	2.10	1.63
Nugget sandstone	2.55	2.40	1.55
Mt. Helen tuff			
Dry	1.47	0.90	1.49
Saturated	1.84	2.17	1.50
Indiana limestone			
Dry	2.28	1.70	2.17
Saturated	2.48	2.75	1.89
Blair dolomite	2.84	4.90[a]	1.30[a]

[a]From Ref. A-8.

Table A-3. Calculated conditions at the HE — test material interface.

Material	U_{m1} (km/s)	P_{m1} (GPa)
Ice	3.35	18.6
West Lebanon glacial till (WLGT)	2.40	30.1
Ottawa banding sand (OWS)	2.51	28.6
Salt	2.27	32.4
Westerly granite	2.21	33.5
Nugget sandstone	2.22	33.2
Mt. Helen tufi		
Dry	2.94	22.8
Saturated	2.56	28.3
Indiana limestone		
Dry	2.94	22.8
Saturated	2.56	28.3
Blair dolomite	1.87	38.9

References

A-1. Ya. B. Zel'dov ch and Yu. P. Raizer, Physics of Shock Waves and High-Temperature Hydrodynamic Phenomana (Academic Press, New York, 1967) Vol. 1, pp. 49-50 and 93-97; Vol. II, pp. 705-709, 710, 726-39 and 846-849.

A-2. C. H. Johansson and P. A. Persson, Detonics of High Explosives (Academic Press, New York, 1970), pp. 18-23, 278-282, 286 and 287-289.

A-3. D. C. Pock, Phil. Mag. 2, 182 (1957).

A-4. W. E. Deal, Phys. Fluids, 1, 523 (1958).

A-5. W. D. Hayes and R. J. Probstein, Hypersonic Flow Theory (Academic Press, New York, 1959), p. 19.

A-6. R. H. Bishop, "Spherical Shock Waves from Underground Explosions," in A. J. Chabai (ed.), Close-In Phenomena of Buried Explosions, Sandia Laboratory, Albuquerque, Rept. SC-4907 (RR) (1963).

A-7. B. M. Dobratz (ed.), Lawrence Livermore Laboratory, Rept. UCRL-51319 (1972).

A-8. N. G. Kalashnikov, M. N. Pavlovskiy, G. V. Simakov and R. J. Trunin, Izv. Akod. Nauk SSSR Fiz. Zemli, No. 2, 23-39 (1973) [Bull. Acad. Sci. USSR, Earth Phys., No. 2, 80-84 (1973)].

VRM/bl/lmc